Leishmania major co-opts IL-7 feedback in monocytes to suppress CD4^{+} T-cell immunity

Yan Fu[1,2], Christophe Toussaint[3], Ina Sauerland[1,2], Elisabeth Reiß[1,2], Lars Philipsen[4], Patricia Gintschel[1,2], Laura Knop[2,5], Andreas Braun[2,6], Bastian Kruse[2,6], Leon-Alexander Dewitz[1,2], Jonas Amore[1,2], Vladyslava Dovhan[2,5], Sönke Weinert[4], Nouria Jantz-Naeem[1,2], Iris Baars[1,2], Juliane Mohr[1,2], Julia Prein[1,2], Cora Schwendele[1,2], Philipp Bruno[2,5], Martin Böttcher[7], Nicole Gröger[8], Hannah Van Hove[9], Melanie Greter[9], Burkhard Becher[9], Sascha Kahlfuß[2,5], Burkhart Schraven[2,5], Robert Geffers[10], Thomas Tüting[2,6], Nicole Joller[11], Stephan Fricke[2,5,12], Antoine-Emmanuel Saliba[3,13,14]*, Thomas Schüler[2,5,14]*, Andreas J. Müller[1,2,14,15]*

[1] Experimental Immunodynamics, Institute for Clinical Immunology and Cell Therapeutics, Medical Faculty, Otto-von-Guericke University Magdeburg, Magdeburg, Germany.

[2] Health Campus Immunology, Infectiology and Inflammation (GCI3) and Center for Health and Medical Prevention (CHaMP), Otto-von-Guericke-University, Magdeburg, Germany

[3] Helmholtz Institute for RNA-based Infection Research, Helmholtz Centre for Infection Research, Würzburg, Germany.

[4] Platform for Multiparametric Bioimaging and Cytometry (MPBIC), Medical Faculty, Otto-von-Guericke-University, Magdeburg, Germany.

[5] Institute for Clinical Immunology and Cell Therapeutics, Medical Faculty, Otto-von-Guericke University Magdeburg, Magdeburg, Germany

[6] Department of Dermatology, Medical Faculty, Otto-von-Guericke University Magdeburg, Magdeburg, Germany.

[7] Department of Hematology, Oncology, and Cell Therapy, Medical Faculty, Otto-von-Guericke University Magdeburg, Magdeburg, Germany.

[8] Department of Zoology/Developmental Neurobiology, Institute of Biology, Otto von Guericke University Magdeburg, Magdeburg, Germany.

[9] Institute of Experimental Immunology, University of Zurich, Switzerland

[10] Helmholtz Centre for Infection Research, Braunschweig, Germany.

[11] Department of Quantitative Biomedicine, University of Zurich, Zurich, Switzerland.

[12] Fraunhofer Institute for Cell Therapy and Immunology, Leipzig, Germany.

[13] University of Würzburg, Faculty of Medicine, Institute of Molecular Infection Biology, Würzburg, Germany.

[14] These authors contributed equally

[15] Lead contact

* Correspondence: emmanuel.saliba@helmholtz-hiri.de (A.E.S.); thomas.schueler@med.ovgu.de (T.S.); andreas.mueller@med.ovgu.de (A.J.M.)

Summary

Effective immunity against infections requires a tight balance between pro- and anti-inflammatory pathways to ensure pathogen clearance while preserving tissue integrity. Intracellular pathogens such as *Leishmania major* can exploit host-cell immunosuppressive functions, yet the underlying molecular and cellular interactions remain incompletely understood. Here we report a monocyte-derived, hypo-inflammatory PDPN^{+}IL-7R^{+} subset that harbours low-proliferating parasites, inhibits effector CD4^{+} T-cell control of intracellular pathogens, and therefore perpetuates infection. This immunosuppression is mediated by fibroblast-derived IL-7, which is up-regulated in response to IFNγ. Thus, our data suggest a cytokine-dependent feedback switch through which IL-7 activates immunosuppressive monocyte-derived cells when local IFNγ production exceeds a critical level. This dampens effector CD4^{+} T cell functions at the expense of pathogen persistence. Targeting this feedback loop may yield novel immunotherapeutic strategies that enhance immune responses while maintaining tissue integrity.

Introduction

Inflammation induces the recruitment of large numbers of monocyte-derived myeloid cells which phagocytose invading pathogens, deliver antimicrobial effector molecules and thus limit pathogen load. However, such cells also exert regulatory functions required for the resolution of inflammation and tissue repair (Guilliams et al., 2018). This is of critical importance for host survival, since unrestrained immune responses endanger tissue integrity and organ function (Ortega-Gomez et al., 2013; Postat et al., 2018; Sugimoto et al., 2016). Intracellular pathogens infecting monocyte-derived cells can interfere with anti-microbial effector functions of their host, thereby establishing long-term persistence and chronic disease (Carvalho et al., 2023; Collins-McMillen et al., 2017; Drewry et al., 2019; Mariotti et al., 2004; Stapels et al., 2018). Furthermore, monocyte-derived cells can acquire an immunosuppressive phenotype that counter-regulates effector functions of other immune cells, or shifts immune responses towards a less inflammatory phenotype (Gundra et al., 2017; Zhang et al., 2022). Elucidating and manipulating these diverse functions holds the potential to improve treatment for infectious diseases (Channappanavar et al., 2016; Dorhoi et al., 2014; Wallis et al., 2023) and cancer (Kruse et al., 2023; Mantovani et al., 2022) but the mechanisms by which such functions are induced and deployed remain incompletely understood.

Upon arrival in the tissue, monocytes adapt their functional properties in response to complex environmental cues, including inflammation- and pathogen-derived signals. This context-dependent adaptation is crucial for a balanced response ensuring pathogen elimination and tissue protection at the same time (Veglia et al., 2021). Thus, within a population of activated monocyte-derived cells, a mixture of pathways triggering inflammatory, antimicrobial, and tissue remodeling functions must be activated (Sanin et al., 2022). Single-cell RNA sequencing (scRNAseq) has been instrumental in dissecting monocytes and their derivatives into phenotypically and functionally distinct subpopulations during infection by intracellular bacterial (Bryson et al., 2019; Hoffman et al., 2021), viral (Baasch et al., 2021) or parasitic (Patir et al., 2020) pathogens, as well as in the tumor microenvironment (Cheng et al., 2021; Mulder et al., 2021). Some of these subpopulations have the capacity to critically divert the course of the disease, even if present only at a small number compared to the total monocyte population

79 (Hoffmann et al., 2022; Zhang et al., 2022). In the course of an infection, the level of complexity is
80 further increased by a significant diversity of virulence, growth rate and invasiveness of individual
81 pathogens, thereby additionally modulating the functional properties of the infected cell type (Avraham
82 et al., 2015; Pisu et al., 2021; Saliba et al., 2016).
83 To address the differential monocyte-derived cell functions in the context of the diverse pathogen states,
84 we employed *Leishmania major* (*L. major*) infection as a physiological model for infection-induced
85 recruitment and activation of monocytes (Heyde et al., 2018; Romano et al., 2017). In this model system,
86 monocyte-derived cells represent the preferential host cell type for intracellular pathogen proliferation
87 and, at the same time, are critical for controlling the parasite through expression of the inducible nitric
88 oxide synthase (iNOS) in response to T cell-derived Interferon-γ (IFNγ) (De Trez et al., 2009; Leon et
89 al., 2007; Muller et al., 2012; Olekhnovitch et al., 2014). Permanent monocyte recruitment to and
90 maturation at the site of infection results in a large phenotypic and functional diversity. Importantly, the
91 proliferation state of the pathogen correlates with the phenotype and function of the infected monocyte-
92 derived cells (Formaglio et al., 2021; Heyde et al., 2018; Mandell and Beverley, 2017). Also, the
93 composition and polarization of these cell populations has been shown to critically impact on the
94 deployment of the anti-*Leishmania* response, e.g. by entertaining type II immune cell circuitries (Lee et
95 al., 2023), or by modulating the reservoir of monocyte-derived cells permissive for pathogen
96 proliferation (Carneiro et al., 2020). However, the cellular and molecular interactions which enable
97 monocyte-derived populations to impact prolongation versus control of the infection remain to be fully
98 elucidated.
99 Here, we combined an *in vivo* pathogen proliferation reporter system with scRNAseq to characterize the
100 function of distinct monocyte-derived subpopulations in the context of their interactions with
101 intracellular pathogens. With the help of this approach, we identified a subset of Podoplanin (PDPN)-
102 and Interleukin-7 receptor (IL-7R) expressing cells which are derived from monocytes and preferentially
103 harbor low-proliferating *L. major*. This PDPN^{+}IL-7R^{+} population exhibited a hypo-inflammatory
104 phenotype and suppressed effector functions of *L. major*-specific CD4^{+} T cells in response to fibroblast-
105 derived IL-7. IL-7 production was dependent on IFNγ release in the course of the adaptive immune
106 response against *L. major*. Interference with IL-7R signaling or depletion of these cells, as well as *Il7*

107 gene inactivation in fibroblasts, resulted in improved effector T cell responses and subsequent pathogen
108 clearance.
109 In summary, we provide evidence for an as-yet unknown feedback loop which dampens T cell responses
110 as a result of the inflammation-associated up-regulation of fibroblast-derived IL-7, and the subsequent
111 immunosuppressive activity of IL-7R^{+} monocyte-derived cells. This mechanism can favour the
112 pathogen to establish persistence and could therefore represent a new target for immunotherapeutic
113 approaches.
114

115 **Results**

116

117 **PDPN^{+}IL-7R^{+} phagocytes infected with low proliferating *L. major* exhibit a hypo-inflammatory**
118 **phenotype**

119 During local immune responses, tissue- and inflammation-derived signals modulate the phenotype and
120 function of recruited immune cells (Romano et al., 2017; Saliba et al., 2016; Szabo et al., 2021; Yamada
121 et al., 2020). However, dissecting these environmental cues has remained challenging. We and others
122 have shown previously that intracellular *L. major* proliferation differs considerably between infected
123 monocyte-derived cells recruited to the infection site (Heyde et al., 2018; Mandell and Beverley, 2017).
124 We therefore utilized pathogen proliferation rate as a proxy for host-pathogen interaction cues which
125 define distinct monocyte-derived cell functions *in vivo*. For this, we employed an *in vivo* proliferation
126 assay, which relies on genetically modified *L. major* parasites expressing the photoconvertible green
127 fluorescence protein mKikume (Lm^{SWITCH}). Upon illumination, mKikume molecules convert from green
128 to red. Consequently, red molecules are preserved in low-proliferating parasites (Lm^{lo}), but are diluted
129 by newly synthesized green molecules in high-proliferating *L. major* (Lm^{hi}) (Fig. 1A) (Formaglio et al.,
130 2021).

131 To characterize the transcriptome of cells which harbour Lm^{lo} and Lm^{hi}, we infected C57BL/6 (B6) mice
132 with 2 x 10^{6} Lm^{SWITCH} in the ear. At 19 days post infection (p.i.), the parasites were photoconverted and
133 CD45^{+} leukocytes were MACS purified 2 days later from the infected ear. Subsequently, single-cell
134 sorting of uninfected, Lm^{lo}- or Lm^{hi}-containing monocyte-derived cells was performed (Fig. 1B). Both
135 CD11c^{int-hi} and Ly6c^{+} were selected to cover a broad spectrum of recruited monocyte-derived cells (Fig.
136 S1A) (Heyde et al., 2018; Olekhnovitch et al., 2014). Lm^{lo}- or Lm^{hi}-infected (termed Lm^{lo}Mo or Lm^{hi}Mo,
137 respectively) as well as uninfected (termed UMo) single monocyte-derived cells were separated using
138 index-sorting into individual wells (Fig. 1C and S1B). ScRNAseq using the SMARTseq2 protocol
139 (Picelli et al., 2013) revealed specifically and consistently high *L. major* transcript counts in cells sorted
140 as infected, but not uninfected (Fig. 1D). In total, 88% of the sorted cells had passed quality control
141 based on mitochondria read counts and percentage of ERCC (Fig. S1C, and see details in Methods).

142 Mapping of the sequenced cells sorted as *Lm*^{hi}Mo (green), UMo (black) and *Lm*^{lo}Mo (red) to a batch-
143 corrected Uniform Manifold Approximation and Projection (UMAP) representation (Fig. 1E, S1D, and
144 S1E) revealed that cells infected with *Lm*^{lo} exhibited a unique gene expression profile. In contrast,
145 uninfected cells and cells infected by *Lm*^{hi} were not distinguishable on the UMAP representation.
146 Unsupervised clustering using the Leiden algorithm identified three distinct clusters of cells referred to
147 as Cluster 1, 2 and 3, with Cluster 3 consisting mainly of *Lm*^{lo}Mo, (Fig. 1F; Table S1).
148 Gene ontology (GO) function terms revealed a differential regulation of mainly immune system-related
149 processes for Cluster 3, but not Cluster 1 and 2. In particular, biological process enrichment in Cluster
150 3 included immunosuppressive signaling pathways, but lowered immune-activating functions and
151 antigen processing as compared to Cluster 1 and 2 (Fig. S1F-G; Table S2-3). Regarding differentially
152 expressed genes (DEG) specific for Cluster 3, we found a strong reduction of the proinflammatory
153 cytokine gene *Il1b*, chemokines and class II MHC-related genes as compared to Cluster 1 and 2. In
154 contrast, cathepsins and immune checkpoint ligands were expressed specifically in Cluster 3, in line
155 with a hypo-inflammatory phenotype suggested by GO terms. Moreover, we found a specific expression
156 of *Pdpn* in Cluster 3, which is reported to be involved in immunomodulatory functions of myeloid cells
157 (Hovd et al., 2024; Rayes et al., 2017). Additionally, *Il7r* was strongly upregulated in Cluster 3. In
158 contrast, *Ccr2* expression was virtually absent in this population (Fig. S1H).
159 As Cluster 3 consisted mainly of *Lm*^{lo}Mo, while *Lm*^{hi}Mo and UMo were evenly dispersed across Cluster
160 1 and 2 (see Fig. 1E), we defined the five most prominent populations for further analysis, i.e. *Lm*^{hi}
161 infected and uninfected cells in Cluster 1 (termed *Lm*^{hi}Mo1 and UMo1) and Cluster 2 (termed *Lm*^{hi}Mo2
162 and UMo2), as well as cells infected with *Lm*^{lo} in Cluster 3 (termed *Lm*^{lo}Mo3) (Fig. 1G). The gene
163 expression pattern specific for Cluster 3 (see Fig. S1H) was consistent with the comparison of *Lm*^{lo}Mo3
164 versus *Lm*^{hi}Mo1, UMo1, *Lm*^{hi}Mo2 and UMo2 (Fig. 1H). This notably included the significantly higher
165 expression of *Pdpn* and *Il7r*, suggesting that PDPN^{+}IL-7R^{+} *Lm*^{lo}Mo3 constitute a hypo-inflammatory
166 cellular subset. These observations were validated by cells sorted according to their differential
167 expression of CD11c (high in Cluster 1), Ly6c (high in cluster 2, intermediate in infected cluster 1)
168 observed during index sorting, and CCR2 (high in cluster 2) observed in scRNAseq (Fig. S1I, and S1J).
169 Quantitative PCR (qPCR) of cells sorted based according to this strategy (Fig. S1K) reproduced the

170 differential gene expression of *Lm*^{lo}Mo3 observed in scRNAseq, including the specific expression of
171 *Pdpn* and *Il7r*, and the hypo-inflammatory phenotype indicated by lower expression of *Il1b*, *Il1r2* and
172 *Ccl5* (Fig. S1I). Also, *Lm*^{lo}Mo3 exhibited the lowest levels of pro-IL-1β, CXCL9 protein among all five,
173 and the lowest IL-6 and IL-12 p35 protein among the infected cell subsets (Fig. 1J). Irrespective of
174 whether we gated *Lm*^{lo}Mo3 cells from the infection gated according to CD11c, Ly6C and CCR2 (see
175 Fig. S1K), or as CD11b^{+}Ly6G^{-}SiglecF^{-} monocytes gated for PDPN and IL-7R expression, *Lm*^{lo}Mo3,
176 PDPN^{+}IL-7R^{+} monocytes, respectively, exhibited a low intracellular pathogen proliferation rate (Fig.
177 S1L-N). These data altogether suggested a PDPN^{+}IL-7R^{+} phagocyte population which is infected with
178 low proliferating *L. major* and which exhibits a hypo-inflammatory phenotype.
179

180 **IL-7R^{+}PDPN^{+} *Lm*^{lo}Mo3 develop from bone-marrow derived CCR2^{+} monocytes and acquire their**
181 **phenotype in the infected tissue**

182 To further characterize the IL-7R^{+}PDPN^{+} *Lm*^{lo}Mo3, we analyzed mannose receptor (CD206) and FcγRI
183 (CD64) expression, which distinguished tissue-resident macrophages, dendritic cells as well as different
184 stages of inflammatory monocytes and monocyte-derived macrophages (Carneiro et al., 2020; Lee et
185 al., 2018; Lee et al., 2023) (Fig. 2A and S2A). Infected IL-7R^{+}PDPN^{+} phagocytes consisted mainly of
186 Ly6C^{int} monocyte-derived macrophages, but hardly any tissue-resident and monocyte-derived dendritic
187 cells (TR/MoDC), nor tissue-resident macrophages (TRM) (Fig. 2B and S2B). The same was observed
188 when analyzing phagocytes infected with low proliferating *L. major* (Fig. 2B and S2C-D). Thus
189 independently of the gating strategy, IL-7R^{+}PDPN^{+} *Lm*^{lo}Mo3 cells seemed to consist mainly of Ly6C^{int-}
190 ^{lo}, monocyte-derived macrophages.

191 Having shown a monocyte-derived phenotype, we sought to determine the dynamics of IL-7R^{+}PDPN^{+}
192 *Lm*^{lo}Mo3 recruitment and turnover. For this, we employed optical time-stamping with mKikume-
193 transgenic mice, in which photoconversion allows the identification of cells recruited before and after a
194 distinct time point (Formaglio et al., 2021; Heyde et al., 2018). The mice were infected with *L. major*
195 expressing blue-fluorescent mTurquoise (*Lm*^{Turquoise}), and mKikume-expressing host cells in the ear were
196 photoconverted at 16 dpi, and analyzed by flow cytometry 5 days later (Fig. 2C). This allowed
197 determining IL-7R and PDPN expression in infected cells and to discriminate photoconverted, long

198 resident (recruited > 5 days before analysis) cells from short resident cells which had been recruited
199 after photoconversion (Fig. 2D and S2E). Importantly, PDPN^{+}IL-7R^{+} cells were found nearly
200 exclusively in the long resident cell fraction, while all other monocyte-derived cells exhibited a higher
201 turnover rate and were recruited mainly after the photoconversion (Fig. 2D and E).
202 Because of their long tissue residence time, we aimed to formally demonstrate whether or not *Lm*^{lo}Mo3
203 derive from CCR2^{+} monocytes. For this, we employed lethally irradiated mice reconstituted with Ccr2-
204 creERT2 (Croxford et al., 2015) x Ai14 (Rosa-CAG-LSL-tdTomato-WPRE) BM, in which *Ccr2*-
205 expressing cells permanently express red fluorescent tdTomato upon Tamoxifen treatment. Tamoxifen
206 was applied either before the infection in order to label cells recruited during the innate wave of
207 monocyte recruitment, or from day 11 p.i. in order to label monocytes recruited during the established
208 adaptive immune response (Carneiro et al., 2020) (Fig. 2F). Tamoxifen treatment induced robust
209 labeling of >75% of blood monocytes for several days (Fig. 2G and S2F). In the infected ear, all
210 monocyte-derived populations, including PDPN^{+}IL-7R^{+}, showed a large proportion of CCR2-dependent
211 tdTomato expressing cells if Tamoxifen was applied during the adaptive wave of monocyte recruitment,
212 but not if the innate wave of monocytes was labeled (Fig. 2H, S2G-H). Therefore, we concluded that
213 despite its low turnover rate as compared to other monocyte-derived cells, the PDPN^{+}IL-7R^{+} *Lm*^{lo}Mo3
214 population was derived from CCR2^{+} inflammatory monocytes recruited to the site of infection.
215
216 **PDPN^{+}IL-7R^{+} *Lm*^{lo}Mo3 dampen T cell responses against *L. major* infection *in vivo***
217 Having shown IL-7R and PDPN expression for monocyte-derived cells in the infected ear, we assessed
218 whether other immune cell types at the infection site, in particular non-myeloid cells, might also include
219 PDPN^{+}IL-7R^{+} double-positive cells (Fig. S3A-C). While as expected, IL-7R was expressed on several
220 leukocyte subsets, PDPN expression, and, consequently, PDPN and IL-7R double-expression, was
221 limited to monocyte-derived, in particular infected, cells (Fig. 3A).
222 Since all IL-7R^{+} monocyte-derived cells co-expressed PDPN, we next employed a *Pdpn-cre* based BM
223 reconstitution approach to specifically abolish IL-7R in these cells (Fig. 3B). For this, we lethally
224 irradiated WT recipient mice, reconstituted them with either *Pdpn-cre* × *Il7r*$^{fl/fl}$ or littermate BM, and
225 infected them with *Lm*^{DsRed} 10 weeks after reconstitution. Pathogen control and effector T cell activation

226 were analyzed at week 3 p.i. We found that IL-7R was significantly diminished in *Lm*^{lo}Mo3, but not in
227 lymph node T cells, confirming monocyte-specific gene deletion of *Il7r* (Fig. 3C and S3D). Strikingly,
228 the *Pdpn-cre* dependent *Il7r* knockout on BM-derived cells significantly reduced *L. major* infected
229 monocytes and pathogen burden (Fig. 3D and S3E). Furthermore, IFNγ production in effector CD4^{+} T
230 cells within the infected ear tissue was elevated (Fig. 3E and S3F), suggesting that disruption of IL-7R
231 signaling in monocyte-derived cells at the site of infection enhances pathogen control by the adaptive
232 immune response. We were able to reproduce the enhanced pathogen control in a different experimental
233 system by reconstituting irradiated recipients with *Rag1*$^{-/-}$× *Il7r*$^{-/-}$ BM and adoptive transfer of WT CD4^{+}
234 (Fig. S3G). The resulting animals, in which IL-7R was exclusively present on lymphocytes, also
235 exhibited enhanced control of *L. major,* confirming the role of IL-7R signaling in non-lymphocyte
236 immune cells (Fig. S3H-I).
237 Enhanced pathogen control in the absence of IL-7R signaling in monocyte-derived cells could be due to
238 cell-intrinsic enhancement of intracellular pathogen control in individual cells devoid of IL-7R, or due
239 to cell-extrinsic effects. In order to address these possibilities, we generated mixed BM chimeras
240 reconstituted with 50% CD45.1 WT and 50% *Il7r*$^{-/-}$ (CD45.2) BM. Mice reconstituted with mixtures of
241 WT CD45.1 and WT CD45.2 BM served as controls (Fig. 3F). We found that infection rates (Fig. 3G),
242 the relative abundance, (Fig. 3H), and the parasite proliferation within (Fig. 3I) the different monocyte-
243 derived cell subsets were independent of the cellular *Il7r* genotype in the mixed BM chimeras.
244 Therefore, we concluded that IL-7R signaling in the IL-7R^{+}PDPN^{+} *Lm*^{lo}Mo3 does not affect their
245 development, abundance, or cell-intrinsic defense function, but dampens pathogen control in a cell-
246 extrinsic manner.
247 Next, we aimed to assess the effect of the depletion of PDPN^{+}IL-7R^{+} *Lm*^{lo}Mo3 on the control of *L.*
248 *major*. For this, we crossed *Pdpn-cre* transgenic mice to iDTR mice expressing the Diphtheria Toxin
249 receptor (DTR) after Cre-mediated elimination of a DNA-STOP cassette (Buch et al., 2005). Using these
250 mice as donors, we created BM chimeras reconstituted with 100% *Pdpn-cre* × iDTR, as well as controls
251 reconstituted with mixed 50% WT (CD45.1) and 50% *Pdpn-cre* × iDTR (CD45.2) BM (Fig. 3J).
252 Diphtheria Toxin (DTX) treatment of mice reconstituted with *Pdpn-cre* × iDTR BM reduced
253 significantly the percentage PDPN^{+} cells among infected phagocytes (Fig. 3K), indicating successful

254 depletion at the site of infection. Importantly, the percentage of infected cells, as well as *L. major* tissue
255 burden was significantly reduced in these animals as compared to non-depleted of only partially
256 depletable BM chimera reconstituted with 50% WT and 50% *Pdpn-cre* × iDTR BM (Fig. 3L and S3J).
257 Of note, this depletion was also associated with an elevated IFNγ production by $CD4^+$ effector T cells
258 (Fig. 3M and S3K). These results underlined an immunosuppressive function of $PDPN^+IL\text{-}7R^+$ Lm^{lo}Mo3
259 in promoting parasite persistence via the inhibition of $CD4^+$ T effector functions. Thus, we concluded
260 that IL-7R signaling in Lm^{lo}Mo3 ultimately resulted in a dampened T cell response against *L. major* and
261 impaired pathogen control.
262
263 **IL-7 from IFNγ-induced fibroblasts establishes a feedback loop that limits the effector T cell**
264 **response in the skin**
265 Stromal cells, particularly fibroblasts, have been shown to produce IL-7 in response to *L. major* infection
266 (Peduto et al., 2009). In line with this, we found that fibroblasts from infected *Pdpn-cre* × $Il7r^{fl/fl}$ BM
267 reconstituted tissues expressed more MHC-I and PD-L1 than controls, indicating their additional
268 activation due to the enhanced immune response (Figure 4A and S4A). The same was observable in
269 *Pdpn-cre* × iDTR BM chimeric mice in which $PDPN^+$ leukocytes were depleted (Fig. 4A and S4B). Of
270 note, we found that *Il7* gene expression was upregulated in the tissue upon *L. major* infection (Fig. 4B
271 and S4C). We therefore sought to elucidate if skin fibroblasts could represent the source of the IL-7
272 modulating the immunosuppressive function of $PDPN^+IL\text{-}7R^+$ Lm^{lo}Mo3. For this, we employed *Prrx-*
273 *cre* × $Il7^{fl/fl}$ mice, which lack *Il7* gene activity in fibroblasts (Knop et al., 2020). Quantitative PCR of
274 stromal cells sorted from the ear confirmed that *Prrx* expression was limited to fibroblasts (Fig. 4C),
275 which were also more abundant in the infected skin than vascular endothelial cells (Fig. 4D and S4D).
276 Additionally, *Il7* expression was significantly reduced in fibroblasts from infected *Prrx-cre* × $Il7^{fl/fl}$
277 mouse ear tissue, but not in any other stromal cell population, further confirming a fibroblast-specific
278 *Il7* gene deficiency (Fig. 4E-F). This suggested that *Prrx-cre* × $Il7^{fl/fl}$ mice indeed lacked *Il7* primarily
279 in fibroblasts in the infected tissue, and that fibroblasts are present in high numbers as compared to
280 vascular endothelial cells as alternative producers of IL-7 (Hara et al., 2012). Importantly, *L. major*
281 clearance was enhanced in *Prrx-cre* × $Il7^{fl/fl}$ mice (Fig. 4G) and IFNγ production by $CD4^+$ T cells was

282 increased (Fig. 4H and S4E). This suggested that fibroblast-derived IL-7 was involved in the suppression
283 of the immune response against *L. major*.
284 IFNγ has been reported to induce IL-7 expression in skin fibroblasts (Dai et al., 2021). Therefore, we
285 hypothesized that enhanced IFNγ production by T cells may contribute to a fibroblast-associated
286 feedback loop, limiting the effectiveness of an initially productive T cell response. This may be a result
287 of IL-7 induction by fibroblasts finally leading to immunosuppression of T cells by PDPN^{+}IL-7R^{+}
288 *Lm*^{lo}Mo3 and subsequent pathogen persistence. In line with this hypothesis, we had shown previously
289 that IFNγ from T cells alone is sufficient for *L. major* containment (Muller et al., 2012), and found T
290 cells represented the main IFNγ producing cell population (Fig. 5A and S5A-B). Also, fibroblasts
291 cultured in the presence of recombinant IFNγ exhibited increased *Il7* cytokine gene expression (Fig.
292 5B). This suggested that T cell-derived IFNγ could stimulate fibroblasts in the infectious environment
293 to produce IL-7.
294 In order to demonstrate the impact of IFNγ signaling on IL-7 production by fibroblasts in vivo, we
295 treated *L. major*-infected mice with IFNγ-specific blocking or isotype-matched control antibodies (Fig.
296 5C). In fibroblasts from the infected tissue of control mice, we observed a strong correlation between
297 *Il7* gene expression and the cellular infection rate. In contrast, this correlation was lost after anti-IFNγ
298 treatment (Fig. 5D). Consequently, anti-IFNγ treatment reduced fibroblasts *Il7* expression in strongly
299 infected tissues (Fig. 5E), and decreased fibroblast activation (Fig. 5F and S5C). Therefore, we
300 concluded that the IFNγ produced during the T cell response against *L. major* induces IL-7 production
301 in fibroblasts, thereby activating immunosuppressive PDPN^{+}IL-7R^{+} *Lm*^{lo}Mo3 which subsequently blunt
302 pathogen clearance.
303
304 **Anti-IL-7/IL-7R treatment results in an enhanced immune response against *L. major***
305 Our data suggested that targeting IL-7R signaling might offer a possibility to prevent
306 immunosuppression by PDPN^{+}IL-7R^{+} *Lm*^{lo}Mo3, thus enhancing effector T cell responses and reducing
307 pathogen burden. Sustained long-term treatment with anti-IL-7R antibody has been shown to impair T
308 cell responses (Colpitts et al., 2009). However, IL-7R has been reported to be critical for maintaining
309 mainly naïve and memory T cells, but less important for effector T cells (Capitini et al., 2009; Fry and

310 Mackall, 2002; Huster et al., 2004). Thus, IL-7/IL-7R-blockade could suspend immunosuppression by
311 PDPN^{+}IL-7R^{+} *Lm*^{lo}Mo3 when applied temporarily during the acute infection.
312 To test if such transient anti-IL-7/IL-7R treatment improves the control of *L. major* infections, we
313 injected *L. major*^{DsRed}-infected mice with an anti-IL-7/IL-7R antibody cocktail after the establishment
314 of infection (Fig. 6A). As expected for IL-7-depleting conditions (Grabstein et al., 1993), the treatment
315 resulted in a decline of immature B cells in the BM and spleen, but not in mature B cells (Fig. S6A-B)
316 three days after antibody injection. We also observed a slight reduction in total CD4^{+} T cells, while the
317 numbers of central memory, effector or regulatory T cells were unchanged in the draining lymph node
318 (Fig. S6C). This indicated that the short-term treatment did not profoundly affect the peripheral
319 lymphocyte homeostasis, or T cell effector populations. Importantly, anti-IL-7/IL-7R treatment resulted
320 within 3-5 days in strongly reduced *L. major* infection (Fig. 6B-C), enhanced IFNγ production by
321 effector T cells (Fig. 6D and S6D), and increased fibroblast activation (Fig.6E and S6E) in the skin. To
322 explore whether anti-IL-7/IL-7R blockade also increased the induction of IFNγ-dependent antimicrobial
323 effector functions (Muller et al., 2012), we determined iNOS expression in monocyte-derived cells
324 isolated from the site of infection and found that anti-IL-7/IL-7R treatment resulted in higher iNOS
325 expression in these cells (Fig.6F and S6F). Collectively, these data indicated that IL-7/IL-7R blockade
326 efficiently increased the adaptive immune response against established skin infections with *L. major*.
327 In order to address whether impaired IL-7R signaling had a long-term effect on pathogen control, and
328 immune activation, we analysed the impact of anti-IL-7/IL-7R treatment several weeks after antibody
329 treatment. For this, *L. major*^{DsRed} infected mice were injected with anti-IL-7/IL-7R antibody or isotype
330 control at day 16 and 20 p.i., and analyzed at week 7 p.i. for pathogen control and immune activation
331 (Fig. 6G). Weekly measurement of the infected ear thickness indicated a transiently higher inflammation
332 in anti-IL-7/IL-7R injected versus control animals, suggesting that the treatment increased the amplitude
333 of the immune response (Fig. 6F). At week 7 p.i., *L. major* tissue burden was reduced compared to
334 isotype control-treated animals (Fig. 6I), indicating that although the local pathology seemed
335 comparable at this late time point, the transient anti-IL-7/IL-7R had a lasting effect on pathogen control.
336 Furthermore, the fraction of IFNγ-producing effector T cells was strongly increased in the draining
337 lymph nodes of anti-IL-7/IL-7R treated animals (Fig. 6J and S6G). These data suggested that the

338 transient blockade of IL-7/IL-7R and suspension of the immunosuppressive function of *Lm*^{lo}Mo3 in the
339 early phase of the response supported a long-lived CD4^{+} T cell response and pathogen control.
340 Altogether, our data therefore indicate that the IL-7 produced by fibroblasts in response to IFNγ drives
341 PDPN^{+}IL-7R^{+} *Lm*^{lo}Mo3 cells blunting CD4^{+} T-cell effector functions, and targeted manipulation of this
342 pathway can facilitate robust anti-*Leishmania major* immunity.
343

344 **Discussion**

345

346 Mechanisms that restrict overshooting effector functions are an important component of immune
347 responses to prevent immunopathological tissue damage (Formaglio et al., 2021; Mishra et al., 2013;
348 Postat et al., 2018; Sugimoto et al., 2016). As such, the effects of IFNγ, a main mediator of cellular
349 immune responses, are controlled on different levels, including the restriction of IFNγ-producing cells
350 (Badovinac et al., 2003) and inhibition of IFNγ signaling (Alexander et al., 1999; Marine et al., 1999).
351 Pathogens can benefit from such regulatory mechanisms to establish efficient infection (Collins-
352 McMillen et al., 2017; Dolgachev et al., 2014; Drewry et al., 2019; Mariotti et al., 2004; Navarro et al.,
353 2011). A better understanding of the cellular and molecular interactions underlying these
354 immunosuppressive functions would greatly facilitate the development of novel immunotherapeutic
355 approaches (Gocher et al., 2022; Wykes and Lewin, 2018). Such approaches have so far mainly focused
356 on T cell functions directly (Ellis et al., 2021), while the potential of monocyte-derived functions is only
357 beginning to be acknowledged (Kruse et al., 2023; Mantovani et al., 2022). We describe here a new self-
358 limiting mechanism by which increasing IFNγ levels initiate a feedback loop that ultimately prompts
359 IL-7R expressing monocyte-derived cells to prevent effector T cells from producing more IFNγ.
360 Interruption of this feedback loop increased effector T cell function and promoted pathogen clearance.
361 Our unbiased identification of a PDPN$^+$IL-7R$^+$ monocyte-derived subset that harbors low-proliferating
362 *L. major* and suppresses CD4$^+$ T-cell effector function adds a new layer to the picture of myeloid cell
363 heterogeneity during chronic infection. The plasticity of myeloid cells at infection sites has been
364 intensely studied, with ample evidence for immunomodulatory functions, for example PD-L2$^+$CD206$^+$
365 monocyte-derived macrophages in the context of helminth infection (Gundra et al., 2017; Gundra et al.,
366 2014; Oyesola et al., 2023), or CD206$^+$ tissue resident macrophages which promote type 2 immunity in
367 non-healing *L. major* Seidman strain infection (Lee et al., 2018; Lee et al., 2020; Lee et al., 2023).
368 Furthermore, CCR2$^+$ monocytes have been shown adopt a dual role in the establishment of parasite-
369 permissive conditions and the activation of parasite control depending on their time point of recruitment
370 and exposure to the local cytokine milieu (Carneiro et al., 2020). Our data extend these concepts by
371 demonstrating that, downstream of IFNγ, stromal fibroblasts secrete IL-7 that engages IL-7R on a

372 PDPN^{+} monocyte-derived population, driving these cells towards a hypo-inflammatory phenotype
373 which dampens CD4^{+} T cell responses.
374 We clearly show that PDPN^{+}IL-7R^{+} *Lm*^{lo}Mo3 cells originate from CCR2^{+} monocytes and have a
375 turnover rate of far more than five days, and do not express TRM markers such as CD206. Thus, we
376 conclude that the functional overlap with alternatively activated CD206^{+} tissue-resident macrophages
377 described previously is at most partial, and that the PDPN^{+}IL-7R^{+} *Lm*^{lo}Mo3 adopt their phenotype upon
378 exposure to the infection site. In line with this, previous reports indicate that both macrophages and
379 monocytes can upregulate cell surface expression of PDPN and IL-7R in response to inflammatory
380 stimuli (Hou et al., 2010; Kerrigan et al., 2012; Yazdani et al., 2024).
381 IL-7R expression by myeloid cells has been shown to promote the development of tissue-resident
382 macrophages in early ontogeny in mice (Cool et al., 2020; Leung et al., 2019). In humans, monocyte-
383 derived lung macrophages have been reported to express IL-7R during their development under non-
384 inflammatory conditions (Evren et al., 2021), and upregulate IL-7R expression in response to
385 inflammation (Al-Mossawi et al., 2019; Hu et al., 2008). Consequently, IL-7R expressing myeloid cells
386 were observed in a variety of inflammatory and infectious diseases. For example, serum from patients
387 infected with *Mycobacterium tuberculosis* (Mtb) as well as Mtb products induces IL-7R on monocytes
388 (Harelimana et al., 2022). Furthermore, a role of IL-7R in monocytes in modulating the immune
389 response has been suggested in human patients of SARS COV2 infection, where their presence in the
390 blood was correlated with lower disease pathology (Zhang et al., 2022). Moreover, *PDPN* and *IL7R*
391 expression was found in monocyte-derived subpopulations of human head and neck carcinoma
392 (Hoffmann et al., 2022), and *IL7R* was found to be a signature gene for tumor-associated monocyte-
393 derived cell subsets in a variety of malignancies (Cheng et al., 2021; Mulder et al., 2021; Nalio Ramos
394 et al., 2022). Altogether, these findings suggest a more general role for IL-7R expressing monocyte-
395 derived cells in dampening immune responses in a variety of infectious diseases, or even beyond. With
396 the identification of a feedback loop fueled by IFNγ, which induces IL-7 production by activated
397 fibroblasts, we provide a multicellular interaction network for the immunosuppressive function of
398 PDPN^{+}IL-7R^{+} *Lm*^{lo}Mo3. Of note, we also observed PDPN^{+}IL-7R^{-} single-positive monocyte-derived
399 cells. These cells might represent an intermediate state, but, alternatively, might deploy

400 immunoregulatory functions independently of the described IL-7 dependent feedback switch, since not
401 only IL-7R, but also PDPN has been shown to be involved in immunoregulatory mechanisms (Xie et
402 al., 2020).
403 The enhancement of pathogen clearance in response to i) *Il7r* deficiency in or depletion of PDPN^{+}IL-
404 7R^{+} *Lm*^{lo}Mo3, ii) fibroblast-specific *Il7* gene inactivation, and iii) IL-7/IL-7R blockade, strongly
405 suggests that IL-7 can mediate an immunosuppressive function. While other cell types could also
406 produce IFNγ to enhance pathogen control, T cells seem to be a main and sufficient IFNγ producer for
407 iNOS induction (Muller et al., 2012), and thereby a very likely target of the described feedback
408 mechanism. At first sight this appears counter-intuitive, since IL-7 stimulates T cell immunity at
409 multiple levels, such as thymic T cell development and the survival of naïve and memory T cells in the
410 periphery. However, this is not the case for effector T cells, which down-regulate IL-7R expression and
411 are thus insensitive to direct IL-7 effects (Bachmann et al., 2005; Huster et al., 2004; Kaech et al., 2003).
412 Importantly, endogenous IL-7 had previously been shown to suppress IFNγ production and to exacerbate
413 disease in a skin infection model of mice with *Schistosoma mansoni* (Wolowczuk et al., 1997).
414 Moreover, treatment with recombinant IL-7 can aggravate *L. major* infection in susceptible mice
415 (Gessner et al., 1995). In line with these reports, we found that short-term blockade of IL-7/IL-7R affects
416 the number of naïve T and B cells in secondary lymphoid organs, but not of effector T cells, whose IFNγ
417 production is increased, resulting in enhanced control of the pathogen. We have shown previously that
418 even slight manipulation of pathogen permissiveness at week 3 p.i. results in enhanced control later on
419 (Formaglio et al., 2021). In line with this, we observed an altered course of pathology, with stronger ear
420 swelling 2-3 weeks after anti-IL-7/IL-7R treatment. The treatment also resulted in more efficient
421 pathogen clearance on the long-term perspective, including stronger IFNγ production by T cells, which
422 indicates a long-lasting effect of the transient anti-IL-7/IL-7R administration at the peak of infection.
423 To specify the critical source of IL-7 mediating an immunosuppressing effect, we employed a
424 conditional *Il7* knockout mediated by *Prrx-cre*, which is active in the majority of skin fibroblasts around
425 birth (Leavitt et al., 2020; Liu et al., 2022), and is upregulated during wound healing (Lee et al., 2022).
426 Importantly, we show that *Il7* expression is affected by the conditional knockout only in fibroblasts, but
427 not any other stromal cell population sorted from the skin. The finding that *Prrx-cre* mediated *Il7* was

428 sufficient to enhance *L. major* clearance and effector $CD4^+$ T cell function therefore suggests that
429 fibroblasts are critical producers of IL-7 in the mechanism. Skin fibroblasts have been shown to increase
430 *Il7* expression in response to inflammation in a variety of models, including the infection of the ear
431 dermis with *L. major* (Peduto et al., 2009), which we could confirm. IFNγ, which we could show to be
432 mainly produced by T cells in our system, is sufficient to induce *Il7* expression upon injection in the
433 skin of uninfected mice. Conversely, anti-IFNγ injection decreases *Il7* expression in a model of
434 autoimmune alopecia (Dai et al., 2021). Therefore, it is conceivable that IFNγ produced by *L. major*-
435 specific T cells (Muller et al., 2012) initiates an IL-7 mediated feedback from fibroblasts which
436 ultimately dampens pathogen clearance. This mechanism might constitute a feedback switch that
437 activates immunosuppressive monocyte-derived cells as soon as local IFNγ production in the course of
438 the T cell response exceeds a certain threshold.
439 Targeting immunoregulatory mechanisms carries the risk of inducing immune-related adverse events
440 (Yan et al., 2024), including pathological effects of unrestricted T cell functions (Byrne and Fisher,
441 2017; Johnson et al., 2016; Murakami et al., 2016). Of note, we did only observe a slight, transient
442 increase of inflammation, while pathogen control was long-lasting. Two explanations are likely for this
443 finding: First, efficient pathogen control could decrease pathogen burden-dependent inflammation
444 (Formaglio et al., 2021), thereby masking the increased immune activation related to impaired IL-7
445 signaling. Second, the effector molecule nitric oxide, which is likely produced at higher amounts in
446 response to the increased IFNγ, can restrict leukocyte recruitment (Mishra et al., 2013; Postat et al.,
447 2018), thus counteracting an even more severe pathology in the anti-IL-7/IL-7R treated animals.
448 Therefore, targeting IL-7 mediated immunosuppression might be especially well-suited for enhancing
449 immune reactions involving nitric oxide-mediated killing by monocyte-derived cells, as nitric oxide
450 seems to provide an additional layer of immunoregulation. Such monocyte-mediated killing has been
451 demonstrated not only in immunity against intracellular pathogens (Olekhnovitch et al., 2014), but also
452 during T cell therapy against cancer (Kruse et al., 2023).
453 Taken together, we describe a cytokine-dependent feedback loop that can restrict T cell activation in
454 response to excessive IFNγ production, a mechanism from which the pathogen can benefit to perpetuate

455 the infection. Targeting this mechanism to adjust the activation of effector T cell functions opens new
456 avenues for future immunotherapeutic approaches.
457

458 **Methods**

459

460 *Ethics Statement*

461 All animal experiments were reviewed and approved by the Ethics Committee of the Office for
462 Veterinary Affairs of the State of Saxony-Anhalt, Germany (permit license numbers 42502-2-1314 UNI
463 MD, 42502-2-1393 Uni MD, 42502-2-1575 Uni MD, 42502-2-1586 Uni MD, 42502-2-1615 Uni MD,
464 42502-2-1672 Uni MD, and 42502-2-1735 Uni MD) in accordance with the legislation of both the
465 European Union (Council Directive 499 2010/63/EU) and the Federal Republic of Germany (according
466 to § 8, Section 1 TierSchG, and TierSchVersV).

467

468 *Parasites, tumor and mouse infections*

469 *L. major* LRC-L137 V121 wild-type, DsRed-, and mKikume-expressing (Lm^{SWITCH}) parasites were
470 described previously (Muller et al., 2013; Sorensen et al., 2003). *L. major* expressing the cyan
471 fluorescent protein mTurquoise ($Lm^{\mathrm{Turquoise}}$) was generated by targeted integration of the mTurquoise
472 gene into the recombinant RNA locus of L. major LRC-L137 V121. For this, the mTurquoise gene
473 (Goedhart et al., 2010) sequence was synthesized *de novo* (Eurofins Scientific) and cloned via BamHI-
474 BglII and NotI (New England Biolabs) into a pLEXSY-Hyg2 vector (Jena Bioscience). The resulting
475 plasmid was linearized usin SwaI (New England Biolabs) and electroporated into *L. major*. Stable
476 transfectants were selected with 30 mg/ml hygromycin B (Invitrogen). Single clones were obtained by
477 limiting dilution. All parasites were grown in M119 medium completed with 10% heat-inactivated fetal
478 calf serum, 0.1 mM adenine, 1 mg/ml biotin, 5 mg/ml hemin, and 2 mg/ml biopterin (all from Sigma)
479 and kept for a maximum of six passages.

480 Wild-type C57BL/6J and CD45.1 (B6.SJL-$Ptprc^{a}Pepc^{b}$/BoyJ, JAX stock #002014) mice, $Il7r^{-/-}$
481 (B6.129S7-$Il7r^{tm1Imx}$/J, JAX stock #002295,) (Peschon et al., 1994), and $Rag1^{-/-}$ (B6.129S7-$Rag1^{tm1Mom}$/J,
482 JAX stock #002096) (Mombaerts et al., 1992) mice were purchased from The Jackson Laboratory (Bar
483 Harbor, ME) via Charles River (Sulzfeld, Germany). Bone marrow from Ccr2-creERT2
484 (C57BL/6NTac-$Ccr2^{tm2982(T2A\text{-}Cre7ESR1\text{-}T2A\text{-}mKate2)BB}$) (Croxford et al., 2015) x Ai14(B6.Cg-
485 $Gt(ROSA)26Sor^{tm14(CAG\text{-}tdTomato)Hze}$) (Madisen et al., 2010) mice was provided by Melanie Greter and

486 Burkhard Becher (University of Zürich, Switzerland). To obtain *Prrx-cre* × *Il7*$^{fl/fl}$ animals, *Prrx-cre*
487 (B6.Cg-Tg(Prrx1-cre)1Cjt/J, JAX stock #005584) (Logan et al., 2002) mice were purchased from The
488 Jackson Laboratory and crossed to mice harboring floxed *Il7* alleles (*Il7*^{fl}*Il7*^{fl}), which had been
489 previously generated by removing a FRT flanked part of a "knockout-first" construct *Il7*$^{tm1a(EUCOMM)Wtsi}$
490 (provided by The European Conditional Mouse Mutagenesis Program (EUCOMM)) using a Flpo-
491 transgenic cross. To obtain *Pdpn-cre* × *Il7r*$^{fl/fl}$ and *Pdpn-cre* × iDTR animals, the sperm of Pdpn-cre
492 mice (C57BL/6N-Tg(Pdpn-icre)14Biat/Biat, EM#11673) (Onder et al., 2011) were purchased from
493 European Mouse Mutant Archive (EMMA) and used in artificial insemination procedures with *Il7r*$^{fl/fl}$
494 (Il7rtm1.1Asin/J, JAX stock #022143) (McCaughtry et al., 2012) females and ROSA26iDTR (CBy.B6-
495 Gt(ROSA)26Sortm1(HBEGF)Awai/J) (Buch et al., 2005) females, respectively. The animals were
496 housed and bred under specific-pathogen-free conditions in the central animal facility (ZTL) of the
497 Medical Faculty at Otto-von-Guericke-Magdeburg, and were used for the experiments in age-and sex-
498 matched groups at an age of 8-14 weeks at the beginning of the experiments. Males were used for
499 experiments involving RNA sequencing, while both males and females were included in the other
500 experiments. No differences in the reported effects were observed between male and female animals.
501 For infection, $2x10^6$ stationary phase promastigotes were washed and resuspended in PBS and
502 subsequently injected in 10 µl into the ear dermis. Where indicated, Tamoxifen (Sigma-Aldrich) was
503 dissolved in olive oil (Sigma-Aldrich) at a concentration of 20 mg/ml and administered by i.p. injection
504 (100 mg/kg) for five consecutive days, either five days before the infection, or between days 11 through
505 15 p.i.
506
507 *Antibody treatment*
508 For anti-IL-7/IL-7R application, mice were intraperitoneally (i.p.) injected with 500 µg of anti-mouse
509 IL-7Rα (clone A7R34, Bio X Cell), which is non-depleting (Mai et al., 2014; Seddon et al., 2003), and
510 500 µg of anti-mouse IL7 (clone M25, Bio X Cell) per treatment (Table S4). Control mice were i.p.
511 injected with 500 µg of rat IgG2a isotype control (clone 2A3, Bio X Cell) and 500 µg of mouse IgG2b
512 isotype control (clone MPC-11, Bio X Cell) per treatment. For anti-IFNγ application, mice were i.p.

513 injected with 500 µg of anti-mouse IFNγ (clone R4-6A2, Bio X Cell) per treatment, while control mice
514 received 500 µg of rat IgG1 isotype control (clone HRPN, Bio X Cell) per treatment.
515
516 *Adoptive T cell and BM transfer, irradiation and BM chimera generation*
517 For adoptive transfer, $CD4^+$ T cells were isolated from axillary, brachial, cervical, and inguinal lymph
518 nodes as well as from the spleen using the CD4 isolation kit and negative selection MACS purification
519 (Miltenyi Biotech, Bergisch Gladbach, Germany) according to the manufacturer's instructions. 1×10^7
520 T cells per recipient were injected intravenously. For BM isolation, BM cells were flushed from tibia
521 and femur with ice-cold non-supplemented RPMI 1640 (PAN Biotec) and filtered through 100 micron
522 cell strainers. Cells were washed with non-supplemented PBS, and 4×10^7 cells (for BM reconstitution)
523 per recipient were resuspended in PBS and injected intravenously into the tail vein. For generating BM
524 chimeras or fully BM reconstituted mice, recipients were γ-irradiated with 9.5 gray before reconstitution
525 and infected 8 weeks later.
526
527 *Photoconversion for proliferation measurement and optical time-stamping*
528 Photoconversion of Lm^{SWITCH} parasites and cells in the mouse ear was performed with a 405 nm
529 wavelength, 665 mW/cm2 collimated high-power LED (Thorlabs). The ears of anesthetized mice were
530 fixed and illuminated from each side for 30 seconds at a distance of 20 cm and were analyzed after 48h
531 by flow cytometry.
532
533 *Flow cytometry*
534 Cells were harvested from digested ears as previously described (Heyde et al., 2018). Draining lymph
535 nodes or spleen were dissociated on a 70 µm cell strainer, and cells were washed with PBS. Surface
536 staining of cells was done by using the antibodies specified in table S4. For intracellular staining of IL-
537 1 beta (Pro-form), IL-6, IL-12 p35, CXCL9, Eomes, Foxp3, GATA3, RORgt, T-bet and IFNγ, the cell
538 suspension was fixed for 1hr at 4°C with fixation buffer (Biolegend), following permeabilization with
539 Perm/Wash solution (Biolegend) according to the manufacturer's instructions and stained with the
540 antibodies liested in table S4 prior to staining and analyzed on a Fortessa flow cytometer (BD

541 Biosciences). Samples with a content of less than 40% of CD11c-expressing cells among $CD45^+$ were
542 excluded from quantitative analysis. The mKikume fluorescence with/without photoconversion was
543 read out at 561 nm excitation and 610/20 nm emission, or 488 nm excitation and 530/30 nm emission,
544 respectively. An autofluorescence signal was recorded at 488 excitation and 695/40 nm emission. Data
545 were analyzed using the FlowJo software (FlowJo, LLC). qPCR of sorted cells was performed as
546 described in the supplemental materials and methods.
547
548 *Single-cell index sorting and SmartSeq2 sequencing library preparation*
549 For scRNAseq, mouse CD45 MicroBeads (Miltenyi Biotec) were used to isolate leukocytes prior to cell
550 surface staining according to manufacturer's instructions. In order to review the complete phenotype of
551 every single cell and associate every phenotype with each sorted single cell, index sorting was performed
552 on FACS ARIA III sorter (BD Biosciences). Single cells were sorted into different wells from a 96-well
553 plate (Costar) filled with 4.65 µl of Buffer RLT Plus (Qiagen), 0.25 µl of SUPERase-In RNase-Inhibitor
554 (Invitrogen), and 0.1 µl of ERCC spike-Mix1 (Invitrogen) pre-diluted 1:500000 in RNAse-free water.
555 For cell-population RNAseq, 50-100 cells per subpopulation per sample were sorted into the wells.
556 Sorted cells were immediately frozen and stored at -80 °C. Single-cell libraries were prepared using
557 Smart-seq2 protocol as previously described (Picelli et al., 2014) with minor modifications: Following
558 cDNA amplification, ACTB expression was measured in each cDNA library by qPCR. All cDNA
559 libraries were diluted aiming to an equivalent ct value for ACTB (average = 21.11, SD = 1.05) and were
560 subsequently used as input for a tagmentation-based protocol (Nextera XT, Illumina) using one quarter
561 of the recommended volumes, 10 min for tagmentation at 55°C (Saliba et al., 2016). Libraries were
562 quantified using Qubit dsDNA Hs Assay (Life Technologies) and fragment size of libraries was
563 analyzed using QIAxcel DNA high resolution Kit (Qiagen) and Bioanalyzer High Sensitivity DNA kit
564 (Agilent). Libraries were normalized to 2 nM and pooled. Particularly, 218 of single-cell libraries or 87
565 of cell-population libraries were sequenced for HiSeq PE200 (Illumina). Sequencing data was analysed
566 as described in the supplemental materials and methods.
567
568 *Processing of RNA sequencing data*

569 Raw fastq files were processed with Cutadapt (v3.7) (Martin, 2011) to remove poly-A tails and adapter
570 sequences from the SMART-seq and Nextera protocols. Low-quality bases (Q-score < 20) and reads left
571 with less than 25 bases after trimming were removed. Sequencing data were mapped to a reference
572 genome using STAR with default parameters (Dobin et al., 2013). The reference genome was built by
573 combining the mouse (GRCm38) and *Leishmania major* (ASM272v2) genomes as well as spike-ins
574 (ERCC92) and the Kikume Green-Red transcript sequences. Raw count matrices were generated from
575 the mapping results after read count quantification with featureCounts (Subread, v1.6.3) (Liao et al.,
576 2014). Two count matrices for 218 single cells and 87 cell-population libraries were created.
577
578 *Quality control and normalization of scRNAseq data*
579 Low-quality cells with more than 2% mitochondrial read counts, more than 20% ERCC spike-ins read
580 counts or less than 1000 detected genes were discarded. Only mouse genes with at least 5 read counts
581 detected in at least 10 cells were retained. Read counts for the 194 retained single-cell transcriptomes
582 were normalized with scNorm (Bacher et al., 2017). Information about the plate for technical biases
583 (*Condition*) and gene length (*WithinSample*) was considered during the normalization procedure.
584
585 *Dimensional reduction and clustering of scRNAseq data*
586 Downstream analysis of the single-cell dataset has been performed with the Seurat R package (v4.0)
587 (Hao et al., 2021). The normalized read count matrix was natural log-transformed and the top 1000
588 highly variables genes were identified (*FindVariableFeatures*). For dimensional reduction, principal
589 component analysis was performed (*RunPCA*) to capture the principal components (PCs) explaining the
590 highest amount of variation in the dataset. Batch effects between mice were corrected with Harmony
591 (v0.1.1). The top 8 PCs from the corrected PCA were projected into a 2D space by Uniform Manifold
592 Approximation Projection (*RunUMAP*) for data visualization. In the uncorrected data, we found that
593 cells from three infected ears were strongly separated from the rest of the cells by in UMAP 1 versus
594 UMAP 2 (see Fig. S1E). MACS-purified cells from these infected ears revealed a substantially lower
595 percentage of CD11c^{+} cells than the remaining samples in other ears. While this war corrected for

596 scRNAseq, we excluded cells from samples with a CD11c$^+$ cell content of less than 40% from
597 experiments with functional readout.
598 A graph-based unsupervised machine learning procedure was used to identify groups of single cells with
599 similar transcriptomes, i.e. clusters. The top 8 PCs were used to build a KNN graph (*FindNeighbors*;
600 k = 10) followed by partition into clusters with the Leiden algorithm (Traag et al., 2019). We used the C
601 implementation for R of the Leiden algorithm (leidenbase v0.1.3, Trapnell Lab) with a resolution set at
602 0.08. Clustering results were used to label cells on the UMAP.
603
604 *Differential expression testing and pathway analysis for single-cell data*
605 Gene markers of each cluster were identified by a Wilcoxon Rank-Sum Test with Seurat
606 (*FindAllMarkers*). Only genes that were expressed in at least 10% of the cells from a given cluster, with
607 an absolute log2 fold-change > 0.25 and a Bonferroni adjusted p-value < 0.05 were considered as
608 differentially expressed.
609 Gene Set Enrichment Analysis (v4.3.2) was used for pathway analysis (Subramanian et al., 2005). DEG
610 testing was repeated over all genes by a Wilcoxon Rank-Sum Test for each cluster versus all others
611 through Seurat (*FindMarkers*). Gene-ranked lists were generated after converting all uncorrected p-
612 values to -log10(p-value) * fold-change direction. Ranked lists were used as input for GSEA preranked
613 with default parameters and Gene Ontology Biological Process gene sets. Pathways up- or down-
614 regulated with FDR < 0.05 were considered significant.
615
616 *Quantitative PCR analysis*
617 For validation of DEG identified in the scRNAseq, 50 cells per sample were sorted from each
618 subpopulation according to the gating strategy shown in Fig. S2C and S2D and lysed in 10µl lysis buffer
619 (RNeasy Plus lysis buffer, QIAGEN) containing 5% SUPERase-In RNase-Inhibitor 20U/µl
620 (Invitrogen). RNA extraction and reverse transcription were performed using the Smart-seq2 protocol
621 as previously described (Picelli et al., 2014). Primers used are specified in table S4.
622 For measuring *Il7* gene expression, total RNA was isolated from *L. major*-infected ear tissue using
623 TRIzol reagent (Invitrogen) and then was reverse-transcribed using the High-Capacity cDNA Reverse

624 Transcription Kit (Applied Biosystems) following the manufacturer's instructions. In order to correct
625 for the immune cell infiltrate which was expected to contain leukocytes expressing *Hprt*, but not *Il7*)
626 *hprt* CT values were corrected according to the mean difference in RNA extracted.
627 For measuring the *Il7* and *Prrx1* gene expression in fibroblasts, LEC and BEC, three replicates of 200
628 cells each were sorted from each mouse ear. RNA extraction and reverse transcription was performed
629 using the Smart-Seq2 protocol as described above. Quantitative PCR analysis was done using a SYBR
630 Green Master Mix (Applied Biosystems).
631 To run the quantitative PCR, 40 cycles of 95 °C (15 s), and 60 °C (60 s) followed by a dissociation
632 protocol 95 °C (15 s), 60 °C (20 s), and 95 °C (15 s) were performed on an ABI Prism 7000 Sequence
633 detection system (Applied Biosystems). Technical triplicates were performed for each sample.
634
635
636 *Limiting dilution assay*
637 *L. major* burden within ear tissue was measured using a limiting dilution assay. Quadruplicate samples
638 of each ear homogenate were serially diluted in 1:2 steps in *Leishmania* culture medium in 96-well
639 plates and incubated at 26 °C for 14 days. The initial parasite burden was calculated from the median of
640 the highest dilutions of the quadruplicates which exhibited parasite growth. In order to compensate
641 experiment-to-experiment variation, the values were normalized to the control groups for pooled data.
642
643 *Proliferation analysis*
644 The proliferation index of *L. major* for flow cytometry was calculated based on the MFI of
645 mKikumeGreen and mKikumeRed as described previously (Heyde et al., 2018). In brief, for visualizing
646 qualitative comparisons within the same sample using the FlowJo software, values were plotted as

647 $$C - 100 * \left(\frac{mKikume\ Red}{mKikume\ Green}\right)_{\text{cell}} / \left(\frac{mKikume\ Red}{mKikume\ Green}\right)_{\text{mean (all infected cells)}}$$

648 with C chosen between 100 and 250 and kept constant within the same sample for which the comparison
649 was made, and the factor 100 was introduced to analyze integer fluorescence values in FlowJo.
650 For inter-sample comparison, the proliferation index was calculated as

651 $$1 - \left(\frac{mKikume\ Red}{mKikume\ Green}\right)_{\text{cell}} / \left(\frac{mKikume\ Red}{mKikume\ Green}\right)_{\text{mean (all infected cells)}}$$

652 and represented as a percent deviation from the total infected cell population within one sample or
653 imaged infection site.
654
655 *Cell culture and stimulation*
656 To generate a fibroblast culture, lymphoid stromal cells were isolated from peripheral lymph nodes of
657 C57BL/6J mice as described previously (Knop et al., 2020). Afterwards, cells from four mice were
658 pooled and seeded in a T25 flask in full medium (RPMI 1640 supplemented with 10% (v/v) FCS (FBS
659 Superior; Sigma) /1% (v/v) P/S (Gibco)/2 mM L-glutamine (Gibco)/1 mM sodium pyruvate (Gibco)/0.1
660 mM HEPES (Gibco)/50 µM 2-mercaptoethanol (Sigma). Cells were cultured for 24h at 37°C and 5%
661 CO_2 and non-attached cells were removed. When reaching confluence, cells were detached using
662 Trypsin/EDTA (Merck Biochrom) and seeded onto T75, and afterwards onto T175. Cells were detached
663 using Trypsin/EDTA and treated with biotinylated anti-CD45 (30-F11, Biolegend) and anti-CD31
664 (MEC13.3, Biolegend)-specific antibodies in degassed staining buffer (PBS/ 2 mM EDTA (Carl Roth)/
665 0,5% (w/v) BSA (AppliChem)) for 15min at 4°C. Cells were washed and resuspended in degassed PBS/
666 2 mM EDTA and CD45+ and CD31+ cells were depleted using Streptavidin MicroBeads (Miltenyi
667 Biotec), LS columns (Miltenyi Biotec) and MidiMACS separator (Miltenyi Biotec) according to
668 manufacturer's instructions. Cells were seeded in a T175 flask in full medium. When reaching
669 confluence, cells were detached using Accutase (Stempro, Gibco) and stained with anti-CD45.2-APC
670 (104, Biolegend), gp38-A488 (8.1.1, Biolegend) and CD31-PE/Cy7 (390, eBioscience)-specific
671 antibodies for 30min at 4°C in staining buffer containing purified anti-CD16/32 (2.4G2 ATCC® HB-
672 197TM). After washing with PBS/2 mM EDTA, cells were resuspended in full medium containing 2
673 µg/ml Ciprobay (Bayer) and $CD45.2^-$ $gp38^+CD31^-$ cells were sorted using FACSARIA III (Becton
674 Dickinson). The sorted cells were seeded at a density of 7400 cells/cm^2 in full medium containing 2
675 µg/ml Ciprobay. After 48h, Ciprobay was removed and the fibroblasts were expanded until reaching
676 confluence in a T175 flask.
677 For IFN-γ stimulation, cells were detached using Accutase and were seeded at 40000 cells/24-Well in
678 500 µl full medium without or with 50 ng/ml recombinant mouse IFN-γ (R&D Systems). After 24h, the

679 cells were detached using Accutase and resuspended in TRIzol reagent (Invitrogen). RNA isolation,
680 reverse transcription and RT-qPCR were performed as described previously (Knop et al., 2020). The
681 following TaqMan® Gene Expression Assays (Thermo Fisher Scientific) were used according to the
682 manufacturer's instructions: Il7 (FAM-MGB probe Mm01295804 m1) and Hprt (FAM-MGB probe
683 Mm00446968 m1). Each sample underwent analysis in triplicates on qTOWER3 G (Analytic Jena).
684 Subsequently, relative quantification was performed according to the ΔCT method.
685
686 *Statistical analysis*
687 Statistical analysis was carried out with GraphPad Prism 8 (GraphPad Software, San Diego, CA, USA).
688 To compare multiple samples in pairwise analysis within datasets with more than two experimental
689 groups, one-way analysis of variance (ANOVA) was done for datasets that had passed a Shapiro-Wilk
690 normal distribution test, Kruskal-Wallis tests were performed for datasets with non-normal distribution.
691 Appropriate multiple comparison post-tests (Bonferroni's for multiple comparisons, Dunnet's for
692 multiple pairwise comparisons or multiple comparisons with a control group in ANOVA, Dunn's test
693 for Kruskal-Wallis analyses) were employed as indicated in the respective Figure legends. Two-group
694 comparisons were analyzed using two-sided, unpaired or paired t-tests for data with normal distribution
695 and Mann-Whitney tests for datasets for which a Shapiro-Wilk normal distribution suggested non-
696 normal distribution. Representation of the median or mean, with standard deviation in cases where not
697 all data points are shown individually, are indicated together with sample size in the Figure legends.
698
699

700 **References**

701

702 Al-Mossawi, H., Yager, N., Taylor, C.A., Lau, E., Danielli, S., de Wit, J., Gilchrist, J., Nassiri, I., Mahe,
703 E.A., Lee, W., *et al.* (2019). Context-specific regulation of surface and soluble IL7R expression by an
704 autoimmune risk allele. Nat Commun *10*, 4575.

705 Alexander, W.S., Starr, R., Fenner, J.E., Scott, C.L., Handman, E., Sprigg, N.S., Corbin, J.E., Cornish,
706 A.L., Darwiche, R., Owczarek, C.M., *et al.* (1999). SOCS1 is a critical inhibitor of interferon gamma
707 signaling and prevents the potentially fatal neonatal actions of this cytokine. Cell *98*, 597-608.

708 Avraham, R., Haseley, N., Brown, D., Penaranda, C., Jijon, H.B., Trombetta, J.J., Satija, R., Shalek,
709 A.K., Xavier, R.J., Regev, A., and Hung, D.T. (2015). Pathogen Cell-to-Cell Variability Drives
710 Heterogeneity in Host Immune Responses. Cell *162*, 1309-1321.

711 Baasch, S., Giansanti, P., Kolter, J., Riedl, A., Forde, A.J., Runge, S., Zenke, S., Elling, R., Halenius,
712 A., Brabletz, S., *et al.* (2021). Cytomegalovirus subverts macrophage identity. Cell *184*, 3774-3793
713 e3725.

714 Bacher, R., Chu, L.F., Leng, N., Gasch, A.P., Thomson, J.A., Stewart, R.M., Newton, M., and
715 Kendziorski, C. (2017). SCnorm: robust normalization of single-cell RNA-seq data. Nat Methods *14*,
716 584-586.

717 Bachmann, M.F., Wolint, P., Schwarz, K., Jager, P., and Oxenius, A. (2005). Functional properties and
718 lineage relationship of CD8+ T cell subsets identified by expression of IL-7 receptor alpha and CD62L.
719 J Immunol *175*, 4686-4696.

720 Badovinac, V.P., Hamilton, S.E., and Harty, J.T. (2003). Viral infection results in massive CD8+ T cell
721 expansion and mortality in vaccinated perforin-deficient mice. Immunity *18*, 463-474.

722 Bryson, B.D., Rosebrock, T.R., Tafesse, F.G., Itoh, C.Y., Nibasumba, A., Babunovic, G.H., Corleis, B.,
723 Martin, C., Keegan, C., Andrade, P., *et al.* (2019). Heterogeneous GM-CSF signaling in macrophages
724 is associated with control of Mycobacterium tuberculosis. Nat Commun *10*, 2329.

725 Buch, T., Heppner, F.L., Tertilt, C., Heinen, T.J., Kremer, M., Wunderlich, F.T., Jung, S., and Waisman,
726 A. (2005). A Cre-inducible diphtheria toxin receptor mediates cell lineage ablation after toxin
727 administration. Nat Methods *2*, 419-426.

728 Byrne, E.H., and Fisher, D.E. (2017). Immune and molecular correlates in melanoma treated with
729 immune checkpoint blockade. Cancer *123*, 2143-2153.

730 Capitini, C.M., Chisti, A.A., and Mackall, C.L. (2009). Modulating T-cell homeostasis with IL-7:
731 preclinical and clinical studies. J Intern Med *266*, 141-153.

732 Carneiro, M.B., Lopes, M.E., Hohman, L.S., Romano, A., David, B.A., Kratofil, R., Kubes, P.,
733 Workentine, M.L., Campos, A.C., Vieira, L.Q., and Peters, N.C. (2020). Th1-Th2 Cross-Regulation
734 Controls Early Leishmania Infection in the Skin by Modulating the Size of the Permissive Monocytic
735 Host Cell Reservoir. Cell Host Microbe *27*, 752-768 e757.

736 Carvalho, A., Ferraz, I.A., Hojo-Souza, N.S., Medeiros, F.A.C., Viana, L.A., Bartholomeu, D.C.,
737 Chaves, A.T., de Souza, T.M., Costa, E.S.M.F., Mendes, T.A.O., *et al.* (2023). Chagas cardiomyopathy
738 is associated with a high susceptibility to T. cruzi infection in monocyte-derived macrophages and a
739 predominance of CD4(+)CD45RO(+) T-cells with immunoregulatory patterns. Acta Trop *237*, 106749.

740 Channappanavar, R., Fehr, A.R., Vijay, R., Mack, M., Zhao, J., Meyerholz, D.K., and Perlman, S. (2016).
741 Dysregulated Type I Interferon and Inflammatory Monocyte-Macrophage Responses Cause Lethal
742 Pneumonia in SARS-CoV-Infected Mice. Cell Host Microbe *19*, 181-193.

743 Cheng, S., Li, Z., Gao, R., Xing, B., Gao, Y., Yang, Y., Qin, S., Zhang, L., Ouyang, H., Du, P., *et al.*
744 (2021). A pan-cancer single-cell transcriptional atlas of tumor infiltrating myeloid cells. Cell *184*, 792-
745 809 e723.

746 Collins-McMillen, D., Stevenson, E.V., Kim, J.H., Lee, B.J., Cieply, S.J., Nogalski, M.T., Chan, G.C.,
747 Frost, R.W., 3rd, Spohn, C.R., and Yurochko, A.D. (2017). Human Cytomegalovirus Utilizes a
748 Nontraditional Signal Transducer and Activator of Transcription 1 Activation Cascade via Signaling
749 through Epidermal Growth Factor Receptor and Integrins To Efficiently Promote the Motility,
750 Differentiation, and Polarization of Infected Monocytes. J Virol *91*.

751 Colpitts, S.L., Dalton, N.M., and Scott, P. (2009). IL-7 receptor expression provides the potential for
752 long-term survival of both CD62Lhigh central memory T cells and Th1 effector cells during Leishmania
753 major infection. J Immunol *182*, 5702-5711.

754 Cool, T., Worthington, A., Poscablo, D., Hussaini, A., and Forsberg, E.C. (2020). Interleukin 7 receptor
755 is required for myeloid cell homeostasis and reconstitution by hematopoietic stem cells. Exp Hematol
756 *90*, 39-45 e33.

757 Croxford, A.L., Lanzinger, M., Hartmann, F.J., Schreiner, B., Mair, F., Pelczar, P., Clausen, B.E., Jung,
758 S., Greter, M., and Becher, B. (2015). The Cytokine GM-CSF Drives the Inflammatory Signature of
759 CCR2+ Monocytes and Licenses Autoimmunity. Immunity *43*, 502-514.

760 Dai, Z., Wang, E.H.C., Petukhova, L., Chang, Y., Lee, E.Y., and Christiano, A.M. (2021). Blockade of
761 IL-7 signaling suppresses inflammatory responses and reverses alopecia areata in C3H/HeJ mice. Sci
762 Adv *7*.

763 De Trez, C., Magez, S., Akira, S., Ryffel, B., Carlier, Y., and Muraille, E. (2009). iNOS-producing
764 inflammatory dendritic cells constitute the major infected cell type during the chronic Leishmania major
765 infection phase of C57BL/6 resistant mice. PLoS Pathog *5*, e1000494.

766 Dobin, A., Davis, C.A., Schlesinger, F., Drenkow, J., Zaleski, C., Jha, S., Batut, P., Chaisson, M., and
767 Gingeras, T.R. (2013). STAR: ultrafast universal RNA-seq aligner. Bioinformatics *29*, 15-21.

768 Dolgachev, V.A., Yu, B., Sun, L., Shanley, T.P., Raghavendran, K., and Hemmila, M.R. (2014).
769 Interleukin 10 overexpression alters survival in the setting of gram-negative pneumonia following lung
770 contusion. Shock *41*, 301-310.

771 Dorhoi, A., Yeremeev, V., Nouailles, G., Weiner, J., 3rd, Jorg, S., Heinemann, E., Oberbeck-Muller, D.,
772 Knaul, J.K., Vogelzang, A., Reece, S.T.*, et al.* (2014). Type I IFN signaling triggers immunopathology
773 in tuberculosis-susceptible mice by modulating lung phagocyte dynamics. Eur J Immunol *44*, 2380-
774 2393.

775 Drewry, L.L., Jones, N.G., Wang, Q., Onken, M.D., Miller, M.J., and Sibley, L.D. (2019). The secreted
776 kinase ROP17 promotes Toxoplasma gondii dissemination by hijacking monocyte tissue migration. Nat
777 Microbiol *4*, 1951-1963.

778 Ellis, G.I., Sheppard, N.C., and Riley, J.L. (2021). Genetic engineering of T cells for immunotherapy.
779 Nat Rev Genet *22*, 427-447.

780 Evren, E., Ringqvist, E., Tripathi, K.P., Sleiers, N., Rives, I.C., Alisjahbana, A., Gao, Y., Sarhan, D.,
781 Halle, T., Sorini, C.*, et al.* (2021). Distinct developmental pathways from blood monocytes generate
782 human lung macrophage diversity. Immunity *54*, 259-275 e257.

783 Formaglio, P., Alabdullah, M., Siokis, A., Handschuh, J., Sauerland, I., Fu, Y., Krone, A., Gintschel, P.,
784 Stettin, J., Heyde, S.*, et al.* (2021). Nitric oxide controls proliferation of Leishmania major by inhibiting
785 the recruitment of permissive host cells. Immunity *54*, 2724-2739 e2710.

786 Fry, T.J., and Mackall, C.L. (2002). Interleukin-7: from bench to clinic. Blood *99*, 3892-3904.

787 Gessner, A., Will, A., Vieth, M., Schroppel, K., and Rollinghoff, M. (1995). Stimulation of B-cell
788 lymphopoiesis by interleukin-7 leads to aggravation of murine leishmaniasis. Immunology *84*, 416-422.

789 Gocher, A.M., Workman, C.J., and Vignali, D.A.A. (2022). Interferon-gamma: teammate or opponent
790 in the tumour microenvironment? Nat Rev Immunol *22*, 158-172.

791 Goedhart, J., van Weeren, L., Hink, M.A., Vischer, N.O., Jalink, K., and Gadella, T.W., Jr. (2010).
792 Bright cyan fluorescent protein variants identified by fluorescence lifetime screening. Nat Methods *7*,
793 137-139.

794 Grabstein, K.H., Waldschmidt, T.J., Finkelman, F.D., Hess, B.W., Alpert, A.R., Boiani, N.E., Namen,
795 A.E., and Morrissey, P.J. (1993). Inhibition of murine B and T lymphopoiesis in vivo by an anti-
796 interleukin 7 monoclonal antibody. J Exp Med *178*, 257-264.

797 Guilliams, M., Mildner, A., and Yona, S. (2018). Developmental and Functional Heterogeneity of
798 Monocytes. Immunity *49*, 595-613.

799 Gundra, U.M., Girgis, N.M., Gonzalez, M.A., San Tang, M., Van Der Zande, H.J.P., Lin, J.D., Ouimet,
800 M., Ma, L.J., Poles, J., Vozhilla, N.*, et al.* (2017). Vitamin A mediates conversion of monocyte-derived
801 macrophages into tissue-resident macrophages during alternative activation. Nat Immunol *18*, 642-653.

802 Gundra, U.M., Girgis, N.M., Ruckerl, D., Jenkins, S., Ward, L.N., Kurtz, Z.D., Wiens, K.E., Tang, M.S.,
803 Basu-Roy, U., Mansukhani, A.*, et al.* (2014). Alternatively activated macrophages derived from
804 monocytes and tissue macrophages are phenotypically and functionally distinct. Blood *123*, e110-122.

805 Hao, Y., Hao, S., Andersen-Nissen, E., Mauck, W.M., 3rd, Zheng, S., Butler, A., Lee, M.J., Wilk, A.J.,
806 Darby, C., Zager, M.*, et al.* (2021). Integrated analysis of multimodal single-cell data. Cell *184*, 3573-
807 3587 e3529.

808 Hara, T., Shitara, S., Imai, K., Miyachi, H., Kitano, S., Yao, H., Tani-ichi, S., and Ikuta, K. (2012).
809 Identification of IL-7-producing cells in primary and secondary lymphoid organs using IL-7-GFP
810 knock-in mice. J Immunol *189*, 1577-1584.

811 Harelimana, J.D., Ahor, H.S., Benner, B., Hellmuth, S., Adankwah, E., Minadzi, D., Aniagyei, W.,
812 Lamptey, M.N.K., Arthur, J., Yeboah, A.*, et al.* (2022). Cytokine-induced transient monocyte IL-7Ra
813 expression and the serum milieu in tuberculosis. Eur J Immunol *52*, 958-969.

814 Heyde, S., Philipsen, L., Formaglio, P., Fu, Y., Baars, I., Hobbel, G., Kleinholz, C.L., Seiss, E.A., Stettin,
815 J., Gintschel, P.*, et al.* (2018). CD11c-expressing Ly6C+CCR2+ monocytes constitute a reservoir for
816 efficient Leishmania proliferation and cell-to-cell transmission. PLoS Pathog *14*, e1007374.

817 Hoffman, D., Tevet, Y., Trzebanski, S., Rosenberg, G., Vainman, L., Solomon, A., Hen-Avivi, S., Ben-
818 Moshe, N.B., and Avraham, R. (2021). A non-classical monocyte-derived macrophage subset provides
819 a splenic replication niche for intracellular Salmonella. Immunity *54*, 2712-2723 e2716.

820 Hoffmann, C., Noel, F., Grandclaudon, M., Massenet-Regad, L., Michea, P., Sirven, P., Faucheux, L.,
821 Surun, A., Lantz, O., Bohec, M.*, et al.* (2022). PD-L1 and ICOSL discriminate human Secretory and
822 Helper dendritic cells in cancer, allergy and autoimmunity. Nat Commun *13*, 1983.

823 Hou, T.Z., Bystrom, J., Sherlock, J.P., Qureshi, O., Parnell, S.M., Anderson, G., Gilroy, D.W., and
824 Buckley, C.D. (2010). A distinct subset of podoplanin (gp38) expressing F4/80+ macrophages mediate
825 phagocytosis and are induced following zymosan peritonitis. FEBS Lett *584*, 3955-3961.

826 Hovd, A.K., Nayar, S., Smith, C.G., Kanapathippillai, P., Iannizzotto, V., Barone, F., Fenton, K.A., and
827 Pedersen, H.L. (2024). Podoplanin expressing macrophages and their involvement in tertiary lymphoid
828 structures in mouse models of Sjogren's disease. Front Immunol *15*, 1455238.

829 Hu, X., Chung, A.Y., Wu, I., Foldi, J., Chen, J., Ji, J.D., Tateya, T., Kang, Y.J., Han, J., Gessler, M.*, et*
830 *al.* (2008). Integrated regulation of Toll-like receptor responses by Notch and interferon-gamma
831 pathways. Immunity *29*, 691-703.

832 Huster, K.M., Busch, V., Schiemann, M., Linkemann, K., Kerksiek, K.M., Wagner, H., and Busch, D.H.
833 (2004). Selective expression of IL-7 receptor on memory T cells identifies early CD40L-dependent
834 generation of distinct CD8+ memory T cell subsets. Proc Natl Acad Sci U S A *101*, 5610-5615.

835 Johnson, D.B., Balko, J.M., Compton, M.L., Chalkias, S., Gorham, J., Xu, Y., Hicks, M., Puzanov, I.,
836 Alexander, M.R., Bloomer, T.L.*, et al.* (2016). Fulminant Myocarditis with Combination Immune
837 Checkpoint Blockade. N Engl J Med *375*, 1749-1755.

838 Kaech, S.M., Tan, J.T., Wherry, E.J., Konieczny, B.T., Surh, C.D., and Ahmed, R. (2003). Selective
839 expression of the interleukin 7 receptor identifies effector CD8 T cells that give rise to long-lived
840 memory cells. Nat Immunol *4*, 1191-1198.

841 Kerrigan, A.M., Navarro-Nunez, L., Pyz, E., Finney, B.A., Willment, J.A., Watson, S.P., and Brown,
842 G.D. (2012). Podoplanin-expressing inflammatory macrophages activate murine platelets via CLEC-2.
843 J Thromb Haemost *10*, 484-486.

844 Knop, L., Deiser, K., Bank, U., Witte, A., Mohr, J., Philipsen, L., Fehling, H.J., Muller, A.J., Kalinke,
845 U., and Schuler, T. (2020). IL-7 derived from lymph node fibroblastic reticular cells is dispensable for
846 naive T cell homeostasis but crucial for central memory T cell survival. Eur J Immunol *50*, 846-857.

847 Kruse, B., Buzzai, A.C., Shridhar, N., Braun, A.D., Gellert, S., Knauth, K., Pozniak, J., Peters, J.,
848 Dittmann, P., Mengoni, M.*, et al.* (2023). CD4(+) T cell-induced inflammatory cell death controls
849 immune-evasive tumours. Nature *618*, 1033-1040.

850 Leavitt, T., Hu, M.S., Borrelli, M.R., Januszyk, M., Garcia, J.T., Ransom, R.C., Mascharak, S.,
851 desJardins-Park, H.E., Litzenburger, U.M., Walmsley, G.G.*, et al.* (2020). Prrx1 Fibroblasts Represent
852 a Pro-fibrotic Lineage in the Mouse Ventral Dermis. Cell Rep *33*, 108356.

853 Lee, K.W., Yeo, S.Y., Gong, J.R., Koo, O.J., Sohn, I., Lee, W.Y., Kim, H.C., Yun, S.H., Cho, Y.B.,
854 Choi, M.A.*, et al.* (2022). PRRX1 is a master transcription factor of stromal fibroblasts for
855 myofibroblastic lineage progression. Nat Commun *13*, 2793.

856 Lee, S.H., Charmoy, M., Romano, A., Paun, A., Chaves, M.M., Cope, F.O., Ralph, D.A., and Sacks,
857 D.L. (2018). Mannose receptor high, M2 dermal macrophages mediate nonhealing Leishmania major
858 infection in a Th1 immune environment. J Exp Med *215*, 357-375.

859 Lee, S.H., Chaves, M.M., Kamenyeva, O., Gazzinelli-Guimaraes, P.H., Kang, B., Pessenda, G., Passelli,
860 K., Tacchini-Cottier, F., Kabat, J., Jacobsen, E.A.*, et al.* (2020). M2-like, dermal macrophages are
861 maintained via IL-4/CCL24-mediated cooperative interaction with eosinophils in cutaneous
862 leishmaniasis. Sci Immunol *5*.

863 Lee, S.H., Kang, B., Kamenyeva, O., Ferreira, T.R., Cho, K., Khillan, J.S., Kabat, J., Kelsall, B.L., and
864 Sacks, D.L. (2023). Dermis resident macrophages orchestrate localized ILC2 eosinophil circuitries to
865 promote non-healing cutaneous leishmaniasis. Nat Commun *14*, 7852.

866 Leon, B., Lopez-Bravo, M., and Ardavin, C. (2007). Monocyte-derived dendritic cells formed at the
867 infection site control the induction of protective T helper 1 responses against Leishmania. Immunity *26*,
868 519-531.

869 Leung, G.A., Cool, T., Valencia, C.H., Worthington, A., Beaudin, A.E., and Forsberg, E.C. (2019). The
870 lymphoid-associated interleukin 7 receptor (IL7R) regulates tissue-resident macrophage development.
871 Development *146*.

872 Liao, Y., Smyth, G.K., and Shi, W. (2014). featureCounts: an efficient general purpose program for
873 assigning sequence reads to genomic features. Bioinformatics *30*, 923-930.

874 Liu, H., Li, P., Zhang, S., Xiang, J., Yang, R., Liu, J., Shafiquzzaman, M., Biswas, S., Wei, Z., Zhang,
875 Z.*, et al.* (2022). Prrx1 marks stem cells for bone, white adipose tissue and dermis in adult mice. Nat
876 Genet *54*, 1946-1958.

877 Logan, M., Martin, J.F., Nagy, A., Lobe, C., Olson, E.N., and Tabin, C.J. (2002). Expression of Cre
878 Recombinase in the developing mouse limb bud driven by a Prxl enhancer. Genesis *33*, 77-80.

879 Madisen, L., Zwingman, T.A., Sunkin, S.M., Oh, S.W., Zariwala, H.A., Gu, H., Ng, L.L., Palmiter, R.D.,
880 Hawrylycz, M.J., Jones, A.R.*, et al.* (2010). A robust and high-throughput Cre reporting and
881 characterization system for the whole mouse brain. Nat Neurosci *13*, 133-140.

882 Mai, H.L., Boeffard, F., Longis, J., Danger, R., Martinet, B., Haspot, F., Vanhove, B., Brouard, S., and
883 Soulillou, J.P. (2014). IL-7 receptor blockade following T cell depletion promotes long-term allograft
884 survival. J Clin Invest *124*, 1723-1733.

885 Mandell, M.A., and Beverley, S.M. (2017). Continual renewal and replication of persistent Leishmania
886 major parasites in concomitantly immune hosts. Proc Natl Acad Sci U S A *114*, E801-E810.

887 Mantovani, A., Allavena, P., Marchesi, F., and Garlanda, C. (2022). Macrophages as tools and targets
888 in cancer therapy. Nat Rev Drug Discov *21*, 799-820.

889 Marine, J.C., Topham, D.J., McKay, C., Wang, D., Parganas, E., Stravopodis, D., Yoshimura, A., and
890 Ihle, J.N. (1999). SOCS1 deficiency causes a lymphocyte-dependent perinatal lethality. Cell *98*, 609-
891 616.

892 Mariotti, S., Teloni, R., Iona, E., Fattorini, L., Romagnoli, G., Gagliardi, M.C., Orefici, G., and Nisini,
893 R. (2004). Mycobacterium tuberculosis diverts alpha interferon-induced monocyte differentiation from
894 dendritic cells into immunoprivileged macrophage-like host cells. Infect Immun *72*, 4385-4392.

895 Martin, M. (2011). Cutadapt removes adapter sequences from high-throughput sequencing reads.
896 EMBnet. journal *17*, 10-12.

897 McCaughtry, T.M., Etzensperger, R., Alag, A., Tai, X., Kurtulus, S., Park, J.H., Grinberg, A., Love, P.,
898 Feigenbaum, L., Erman, B., and Singer, A. (2012). Conditional deletion of cytokine receptor chains
899 reveals that IL-7 and IL-15 specify CD8 cytotoxic lineage fate in the thymus. J Exp Med *209*, 2263-
900 2276.

901 Mishra, B.B., Rathinam, V.A., Martens, G.W., Martinot, A.J., Kornfeld, H., Fitzgerald, K.A., and
902 Sassetti, C.M. (2013). Nitric oxide controls the immunopathology of tuberculosis by inhibiting NLRP3
903 inflammasome-dependent processing of IL-1beta. Nat Immunol *14*, 52-60.

904 Mombaerts, P., Iacomini, J., Johnson, R.S., Herrup, K., Tonegawa, S., and Papaioannou, V.E. (1992).
905 RAG-1-deficient mice have no mature B and T lymphocytes. Cell *68*, 869-877.

906 Mulder, K., Patel, A.A., Kong, W.T., Piot, C., Halitzki, E., Dunsmore, G., Khalilnezhad, S., Irac, S.E.,
907 Dubuisson, A., Chevrier, M.*, et al.* (2021). Cross-tissue single-cell landscape of human monocytes and
908 macrophages in health and disease. Immunity *54*, 1883-1900 e1885.

909 Muller, A.J., Aeschlimann, S., Olekhnovitch, R., Dacher, M., Spath, G.F., and Bousso, P. (2013).
910 Photoconvertible pathogen labeling reveals nitric oxide control of Leishmania major infection in vivo
911 via dampening of parasite metabolism. Cell Host Microbe *14*, 460-467.

912 Muller, A.J., Filipe-Santos, O., Eberl, G., Aebischer, T., Spath, G.F., and Bousso, P. (2012). CD4+ T
913 cells rely on a cytokine gradient to control intracellular pathogens beyond sites of antigen presentation.
914 Immunity *37*, 147-157.

915 Murakami, N., Borges, T.J., Yamashita, M., and Riella, L.V. (2016). Severe acute interstitial nephritis
916 after combination immune-checkpoint inhibitor therapy for metastatic melanoma. Clin Kidney J *9*, 411-
917 417.

918 Nalio Ramos, R., Missolo-Koussou, Y., Gerber-Ferder, Y., Bromley, C.P., Bugatti, M., Nunez, N.G.,
919 Tosello Boari, J., Richer, W., Menger, L., Denizeau, J.*, et al.* (2022). Tissue-resident FOLR2(+)
920 macrophages associate with CD8(+) T cell infiltration in human breast cancer. Cell *185*, 1189-1207
921 e1125.

922 Navarro, S., Cossalter, G., Chiavaroli, C., Kanda, A., Fleury, S., Lazzari, A., Cazareth, J., Sparwasser,
923 T., Dombrowicz, D., Glaichenhaus, N., and Julia, V. (2011). The oral administration of bacterial extracts
924 prevents asthma via the recruitment of regulatory T cells to the airways. Mucosal Immunol *4*, 53-65.

925 Olekhnovitch, R., Ryffel, B., Muller, A.J., and Bousso, P. (2014). Collective nitric oxide production
926 provides tissue-wide immunity during Leishmania infection. J Clin Invest *124*, 1711-1722.

927 Onder, L., Scandella, E., Chai, Q., Firner, S., Mayer, C.T., Sparwasser, T., Thiel, V., Rulicke, T., and
928 Ludewig, B. (2011). A novel bacterial artificial chromosome-transgenic podoplanin-cre mouse targets
929 lymphoid organ stromal cells in vivo. Front Immunol *2*, 50.

930 Ortega-Gomez, A., Perretti, M., and Soehnlein, O. (2013). Resolution of inflammation: an integrated
931 view. EMBO Mol Med *5*, 661-674.

932 Oyesola, O.O., Hilligan, K.L., Namasivayam, S., Howard, N., Clancy, C.S., Zhao, M., Oland, S.D.,
933 Kiwanuka, K.N., Garza, N.L., Lafont, B.A.P.*, et al.* (2023). Exposure to lung-migrating helminth
934 protects against murine SARS-CoV-2 infection through macrophage-dependent T cell activation. Sci
935 Immunol *8*, eadf8161.

936 Patir, A., Gossner, A., Ramachandran, P., Alves, J., Freeman, T.C., Henderson, N.C., Watson, M., and
937 Hassan, M.A. (2020). Single-cell RNA-seq reveals CD16(-) monocytes as key regulators of human
938 monocyte transcriptional response to Toxoplasma. Sci Rep *10*, 21047.

939 Peduto, L., Dulauroy, S., Lochner, M., Spath, G.F., Morales, M.A., Cumano, A., and Eberl, G. (2009).
940 Inflammation recapitulates the ontogeny of lymphoid stromal cells. J Immunol *182*, 5789-5799.

941 Peschon, J.J., Morrissey, P.J., Grabstein, K.H., Ramsdell, F.J., Maraskovsky, E., Gliniak, B.C., Park,
942 L.S., Ziegler, S.F., Williams, D.E., Ware, C.B.*, et al.* (1994). Early lymphocyte expansion is severely
943 impaired in interleukin 7 receptor-deficient mice. J Exp Med *180*, 1955-1960.

944 Picelli, S., Bjorklund, A.K., Faridani, O.R., Sagasser, S., Winberg, G., and Sandberg, R. (2013). Smart-
945 seq2 for sensitive full-length transcriptome profiling in single cells. Nat Methods *10*, 1096-1098.

946 Picelli, S., Faridani, O.R., Bjorklund, A.K., Winberg, G., Sagasser, S., and Sandberg, R. (2014). Full-
947 length RNA-seq from single cells using Smart-seq2. Nat Protoc *9*, 171-181.

948 Pisu, D., Huang, L., Narang, V., Theriault, M., Le-Bury, G., Lee, B., Lakudzala, A.E., Mzinza, D.T.,
949 Mhango, D.V., Mitini-Nkhoma, S.C.*, et al.* (2021). Single cell analysis of M. tuberculosis phenotype
950 and macrophage lineages in the infected lung. J Exp Med *218*.

951 Postat, J., Olekhnovitch, R., Lemaitre, F., and Bousso, P. (2018). A Metabolism-Based Quorum Sensing
952 Mechanism Contributes to Termination of Inflammatory Responses. Immunity *49*, 654-665 e655.

953 Rayes, J., Lax, S., Wichaiyo, S., Watson, S.K., Di, Y., Lombard, S., Grygielska, B., Smith, S.W.,
954 Skordilis, K., and Watson, S.P. (2017). The podoplanin-CLEC-2 axis inhibits inflammation in sepsis.
955 Nat Commun *8*, 2239.

956 Romano, A., Carneiro, M.B.H., Doria, N.A., Roma, E.H., Ribeiro-Gomes, F.L., Inbar, E., Lee, S.H.,
957 Mendez, J., Paun, A., Sacks, D.L., and Peters, N.C. (2017). Divergent roles for Ly6C+CCR2+CX3CR1+
958 inflammatory monocytes during primary or secondary infection of the skin with the intra-phagosomal
959 pathogen Leishmania major. PLoS Pathog *13*, e1006479.

960 Saliba, A.E., Li, L., Westermann, A.J., Appenzeller, S., Stapels, D.A., Schulte, L.N., Helaine, S., and
961 Vogel, J. (2016). Single-cell RNA-seq ties macrophage polarization to growth rate of intracellular
962 Salmonella. Nat Microbiol *2*, 16206.

963 Sanin, D.E., Ge, Y., Marinkovic, E., Kabat, A.M., Castoldi, A., Caputa, G., Grzes, K.M., Curtis, J.D.,
964 Thompson, E.A., Willenborg, S.*, et al.* (2022). A common framework of monocyte-derived macrophage
965 activation. Sci Immunol *7*, eabl7482.

966 Seddon, B., Tomlinson, P., and Zamoyska, R. (2003). Interleukin 7 and T cell receptor signals regulate
967 homeostasis of CD4 memory cells. Nat Immunol *4*, 680-686.

968 Sorensen, M., Lippuner, C., Kaiser, T., Misslitz, A., Aebischer, T., and Bumann, D. (2003). Rapidly
969 maturing red fluorescent protein variants with strongly enhanced brightness in bacteria. FEBS Lett *552*,
970 110-114.

971 Stapels, D.A.C., Hill, P.W.S., Westermann, A.J., Fisher, R.A., Thurston, T.L., Saliba, A.E.,
972 Blommestein, I., Vogel, J., and Helaine, S. (2018). Salmonella persisters undermine host immune
973 defenses during antibiotic treatment. Science *362*, 1156-1160.

974 Subramanian, A., Tamayo, P., Mootha, V.K., Mukherjee, S., Ebert, B.L., Gillette, M.A., Paulovich, A.,
975 Pomeroy, S.L., Golub, T.R., Lander, E.S., and Mesirov, J.P. (2005). Gene set enrichment analysis: a
976 knowledge-based approach for interpreting genome-wide expression profiles. Proc Natl Acad Sci U S
977 A *102*, 15545-15550.

978 Sugimoto, M.A., Sousa, L.P., Pinho, V., Perretti, M., and Teixeira, M.M. (2016). Resolution of
979 Inflammation: What Controls Its Onset? Front Immunol *7*, 160.

980 Szabo, P.A., Dogra, P., Gray, J.I., Wells, S.B., Connors, T.J., Weisberg, S.P., Krupska, I., Matsumoto,
981 R., Poon, M.M.L., Idzikowski, E.*, et al.* (2021). Longitudinal profiling of respiratory and systemic
982 immune responses reveals myeloid cell-driven lung inflammation in severe COVID-19. Immunity *54*,
983 797-814 e796.

984 Traag, V.A., Waltman, L., and van Eck, N.J. (2019). From Louvain to Leiden: guaranteeing well-
985 connected communities. Sci Rep *9*, 5233.

986 Veglia, F., Sanseviero, E., and Gabrilovich, D.I. (2021). Myeloid-derived suppressor cells in the era of
987 increasing myeloid cell diversity. Nat Rev Immunol *21*, 485-498.

988 Wallis, R.S., O'Garra, A., Sher, A., and Wack, A. (2023). Host-directed immunotherapy of viral and
989 bacterial infections: past, present and future. Nat Rev Immunol *23*, 121-133.

990 Wolowczuk, I., Delacre, M., Roye, O., Giannini, S.L., and Auriault, C. (1997). Interleukin-7 in the skin
991 of Schistosoma mansoni-infected mice is associated with a decrease in interferon-gamma production
992 and leads to an aggravation of the disease. Immunology *91*, 35-44.

993 Wykes, M.N., and Lewin, S.R. (2018). Immune checkpoint blockade in infectious diseases. Nat Rev
994 Immunol *18*, 91-104.

995 Xie, Z., Shao, B., Hoover, C., McDaniel, M., Song, J., Jiang, M., Ma, Z., Yang, F., Han, J., Bai, X.*, et*
996 *al.* (2020). Monocyte upregulation of podoplanin during early sepsis induces complement inhibitor
997 release to protect liver function. JCI Insight *5*.

998 Yamada, K.J., Heim, C.E., Xi, X., Attri, K.S., Wang, D., Zhang, W., Singh, P.K., Bronich, T.K., and
999 Kielian, T. (2020). Monocyte metabolic reprogramming promotes pro-inflammatory activity and
1000 Staphylococcus aureus biofilm clearance. PLoS Pathog *16*, e1008354.

1001 Yan, T., Yu, L., Zhang, J., Chen, Y., Fu, Y., Tang, J., and Liao, D. (2024). Achilles' Heel of currently
1002 approved immune checkpoint inhibitors: immune related adverse events. Front Immunol *15*, 1292122.

1003 Yazdani, R., Askari, M., Ahmadi, A.M., Azizi, G., Ciric, B., Boehm, A., Zhang, G.X., and Rostami, A.
1004 (2024). Mouse monocytes express CD127 by immune cells, not LPS. Front Immunol *15*, 1356004.

1005 Zhang, B., Zhang, Y., Xiong, L., Li, Y., Zhang, Y., Zhao, J., Jiang, H., Li, C., Liu, Y., Liu, X.*, et al.*
1006 (2022). CD127 imprints functional heterogeneity to diversify monocyte responses in inflammatory
1007 diseases. J Exp Med *219*.

1008

Acknowledgments: The helpful discussions with Tim Lämmermann, Tatjana Ruhl, Gabriel Sollberger, and all members of the Institute of Molecular and Clinical Immunology are gratefully acknowledged. We thank Tamas Dolowschiak for invaluable advice for setting up the scRNAseq library construction. We also thank Roland Hartig from the MPBIC platform and the team of the ZTL of the Medical Faculty OvGU for excellent technical support, and Ehsan Vafadarnejad for the support with initial scRNAseq data analysis.

Funding: This work was supported by funding from the European Research Council (ERC) under the European Union's Horizon 2020 research and innovation program (StG ImmProDynamics, grant agreement 714233 to A.J.M and grant 677200 to N.J.), the German Research Foundation (DFG) (SFB854-B31, MU3744/6-1, and SPP2225 EXIT (MU3744/5-1)).

Author contributions: YF, TS, AES and AJM conceived of and designed the study. YF, IS, ER, LP, PG, LK, BK, LAD, VD, JA, NJN, MB, IB, JM, JP, CS, BP, and AJM conducted experiments, YF, ER, CT, LP, JM, SK, LK, BK, SF, AB, RG and AJM analyzed the data. NG, TT, BS, HVH, MG, BB, NJ, and TS provided critical technology. YF, TS, AES and AJM wrote the manuscript. All authors revised, commented and approved the manuscript.

Competing interests: The authors declare no competing interests.

Data and materials availability: RNAseq data supporting the findings of this study have been deposited at Gene Expression Omnibus under accession no. GSE228455. R scripts used for the analysis of the scRNAseq data are available on GitHub: https://github.com/saliba-lab/Monocytes_leishmania

1034 **Figure legends**

1035

1036 **Figure 1.**

1037 **PDPN^{+}IL-7R^{+} phagocytes infected with low proliferating *L. major* exhibit a hypo-inflammatory**

1038 **phenotype.**

1039 **A.** Experimental setup for *in vivo L. major* proliferation measurement using *Lm*^{SWITCH}. **B.** Experimental

1040 setup for index single-cell sorting of CD11c^{int-hi} and Ly6c^{+} monocytes from 10 individual mouse ears

1041 infected with proliferation reporter parasites at 3 weeks post-infection (p.i.). **C.** Index mKikume red and

1042 green reporter fluorescence values. **D.** *L. major* reads detected in the sorted monocytes infected with

1043 high (green) or low (red) proliferating pathogen, or uninfected (black). **E.** UMAP representation and

1044 mapping of cells sorted as high-proliferator infected (green), uninfected (black) and low-proliferator

1045 infected (red). **F.** Leiden clustering of the scRNAseq data on the UMAP representation. **G.** Fraction of

1046 monocytes sorted as infected with *Lm*^{hi} (green), uninfected (black) or infected with *Lm*^{lo} (red) among

1047 the three clusters identified by the Leiden algorithm. The five highlighted most prominent populations

1048 (*Lm*^{hi}Mo1, UMo1, Cluster 1; *Lm*^{hi}Mo2, Umo2, Cluster 2; *Lm*^{lo}Mo3, Cluster 3) were selected for

1049 differentially expressed gene (DEG) analysis. **H.** Normalized expression (color-code) and cell fraction

1050 per population with detected expression (circle size) for selected DEG differentially expressed in

1051 *Lm*^{lo}Mo3 versus all other populations. **I.** Quantitative PCR (qPCR) analysis of selected genes identified

1052 by scRNAseq. Expression levels were determined for replicates of 50-100 cells sorted according to the

1053 gating strategy outlined in Fig. S1K. Expression levels relative to *Gapdh* and normalized to *Lm*^{lo}Mo3

1054 are shown. Each symbol represents 50-100 cell replicates; data was generated from two independent

1055 experiments. Horizontal lines denote the median. ****, $p<0.0001$;***, $p<0.001$;**, $p<0.01$;*, $p<0.05$

1056 compared to the *Lm*^{lo}Mo3 population according to one-way ANOVA with Dunnett's post-test. **J.** Mean

1057 fluorescence intensity (MFI) of pro-IL-1β, CXCL9, IL-6, and IL-12 p35 among the *Lm*^{hi}Mo1, Umo1,

1058 *Lm*^{hi}Mo2, Umo2, and *Lm*^{lo}Mo3 (according to the gating strategy shown in Fig. S1K) from *L. major*

1059 infected C56BL/6J mouse ear skin at 3 weeks p.i. Each dot represents one infected ear analyzed, data

1060 pooled from two independent experiments. Horizontal lines denote mean. ****, $p<0.0001$; **, $p<0.01$;

1061 *, $p<0.05$ according to one-way ANOVA multiple comparison with Dunnett's post-test.

1062

1063

1064 **Figure 2. IL-7R^{+}PDPN^{+} *Lm*^{lo}Mo3 develop from bone-marrow derived CCR2^{+} monocytes and**
1065 **acquire their phenotype in the infected tissue.**

1066 **A.** Gating to determine tissue-resident and monocyte-derived dendritic cells (TR/MoDC), tissue-
1067 resident macrophages (TRM) and different monocyte-derived populations (left) and proportion of these
1068 populations among CD11b^{+}Ly6G^{-}SiglecF^{-} phagocytes (right). **B.** Proportion of the cell populations
1069 shown in (A) among *Lm*^{hi}Mo1, Umo1, *Lm*^{hi}Mo2, Umo2, and *Lm*^{lo}Mo3 (H) and among infected
1070 CD11b^{+}Ly6G^{-}SiglecF^{-} cells with differential PDPN and IL-7R expression and different intracellular
1071 pathogen proliferation rates. Horizontal lines denote the median. Each dot represents one infected ear
1072 analyzed, data pooled from two independent experiments. **C.** Experimental approach to identify newly
1073 recruited monocytes by photoconversion of mKikume transgenic mice (left). **D.** Upper left: Infected
1074 CD11b^{+}Ly6G^{-}SiglecF^{-} cells from *Lm*^{Turquoise}-infected ear tissue at 3 weeks p.i. from mKikume transgenic
1075 mice before (green curve) and 0 h after photoconversion (red curve). Lower left: Identification of short
1076 resident mKikume green (recruited <5 days after photoconversion) and long resident mKikume red
1077 (recruited >5 days after photoconversion) cells among infected CD11b^{+}Ly6G^{-}SiglecF^{-} cells. Right:
1078 Examples of the proportion long resident cells (mKikume red^{+}) among infected CD11b^{+}Ly6G^{-}SiglecF^{-}
1079 cells with differential PDPN and IL-7R expression. **E.** Quantification of short and long resident cells
1080 among infected CD11b^{+}Ly6G^{-}SiglecF^{-} cells with differential PDPN and IL-7R expression. Horizontal
1081 lines denote the median. Each dot represents one infected analyzed ear, data pooled from two
1082 independent experiments. **F.** Experimental approach to demonstrate the origin of *Lm*^{lo}Mo3 from bone
1083 marrow-derived, CCR2^{+} monocytes recruited during the innate and adaptive phase of the anti-
1084 *Leishmania* response. **G.** CCR2-cre^{ER}-dependent TdTomato expression in different blood leukocytes
1085 cells before, and at day 2, 6 and 23 after the beginning of five daily Tamoxifen injections. Horizontal
1086 lines denote the median. Each dot represents one animal, data pooled from two independent experiments.
1087 **H.** Fraction of CCR2-cre^{ER}-dependent tdTomato expressing cells among PDPN and IL-7R expressing
1088 monocyte-derived cells. The cre recombinase activity was induced in CCR2^{+} monocytes for the innate
1089 phase of the immune response by injecting Tamoxifen before infection (left), or for the adaptive phase

1090 by injection at 11-15 days p.i. (right). Horizontal lines denote the median. Each symbol represents one
1091 infection site per condition obtained from two independent experiments.
1092
1093 **Figure 3. PDPN$^+$IL-7R$^+$ *Lm*^{lo}Mo3 dampen T cell responses against *L. major* infection *in vivo*.**
1094 **A**. Proportion of PDPN$^-$IL-7R$^+$ (left), PDPN$^+$ IL-7R$^-$ (middle) and PDPN$^+$IL-7R$^+$ (right) fractions among
1095 different leukocytes at the infection site at week 3 p.i. Bars denote the median. Each symbol represents
1096 one infection site per condition obtained from two independent experiments. **B.** Experimental setup for
1097 cell-specific *Il7r*-deficiency in PDPN$^+$ leukocytes. **C.** Validation of cell-specific IL-7R deficiency.
1098 Upper panels: Example and MFI analysis for IL-7R surface expression on *Lm*^{lo}Mo3 (gated according to
1099 figure S1K) in the infected ear tissue at 3 weeks p.i. Lower panels: Example and MFI analysis of IL-7R
1100 expression on CD4$^+$ T cells in the draining lymph node (dLN) at week 3 p.i. Values are normalized to
1101 control animals. Each dot represents one infected ear or dLN analyzed. Isotype control-stained samples
1102 are shown as a grey histogram and dashed line in the data plot, respectively. Horizontal lines denote
1103 mean, data pooled from 2 independent experiments. **, $p<0.01$; ns, not significant according to unpaired
1104 t-test. **D.** *L. major*-infected cell fraction among recruited monocytes in the ear tissue (left) and limiting
1105 dilution assay (LDA) of *L. major* tissue burden normalized to control animals (right) at week 3 p.i. of
1106 lethally irratiated mice either reconstituted with littermate control (black symbols) or *Pdpn-cre* × *Il7r*$^{fl/fl}$
1107 BM (blue symbols). **E.** IFNγ$^+$ fraction and IFNγ MFI among effector CD4$^+$ T cells within *L. major*-
1108 infected ear at week 3 p.i.for mice reconstituted with either littermate control (black symbols) or *Pdpn-*
1109 *cre* × *Il7r*$^{fl/fl}$ BM (blue symbols). Each symbol in (D-E) represents one individual mouse ear. Horizontal
1110 lines denote the mean. ***, $p<0.001$; **, $p<0.01$; *, $p<0.05$ according to unpaired t-test. Data
1111 representative of two independent experiments. **F.** Experimental setup for mixed BM chimera
1112 reconstituted with 50% CD45.1 WT and 50% *Il7r*$^{-/-}$ (CD45.2) BM. Mice reconstituted with mixtures of
1113 WT CD45.1 and WT CD45.2 BM served as controls. **G.** *L. major* infected cell fraction among recruited
1114 monocytes in the ear tissue at week 3 p.i., either WT BM chimera compartment (black symbols), or *Il7r*$^-$
1115 $^{/-}$ BM chimera compartment (blue symbols). **H.** Fraction of *Lm*^{hi}Mo1, *Lm*^{hi}Mo2, and *Lm*^{lo}Mo3 (gated
1116 according to figure S1K) among monocyte-derived cells of each BM chimera compartment, either WT
1117 BM chimera compartment (closed symbols), or *Il7r*$^{-/-}$ BM chimera compartment (open symbols) within

1118 *L. major* infected ear tissue at 3 week p.i. Each symbol represents one individual mouse ear, data pooled
1119 from two independent experiments. Horizontal lines denote the median. No significance detected
1120 according to one-way ANOVA multiple comparison with Dunn's post-test. **I**. Intracellular pathogen
1121 proliferation rates among *Lm*^{hi}Mo1, *Lm*^{hi}Mo2, and *Lm*^{lo}Mo3 (gated according to figure S1K), either WT
1122 BM chimera compartment (closed symbols), or *Il7r*$^{-/-}$ BM chimera compartment (open symbols). Each
1123 symbol represents one individual mouse ear, data pooled from two independent experiments. Horizontal
1124 lines denote the median. ****, $p<0.0001$ according to one-way ANOVA multiple comparison with
1125 Dunnett post-test. **J.** Experimental setup for depletion of *Pdpn*-expressing leukocytes of lethally
1126 irradiated mice reconstituted with either *Pdpn-cre* × iDTR BM cells, or 50% of *Pdpn-cre* × iDTR and
1127 50% of CD45.1 WT BM cells. **K.** Validation of depletion of PDPN^{+} cells among infected leukocytes.
1128 Upper panel: Example of PDPN staining of infected cells from ear tissue at 3 weeks p.i. in depleted
1129 (blue curve) or non-depleted control animals (black curve). Lower panel: Percentage of PDPN^{+} cells
1130 among infected leukocytes from ear tissue at 3 weeks p.i. in depleted (blue symbols) or non-depleted
1131 control animals (black symbols). Horizontal lines denote the mean. Each dot represents one infected ear
1132 analyzed. *, $p<0.05$; ns, not significant according to unpaired t-test. **L.** *L. major* infected phagocyte
1133 fraction (left) and *L. major* burden (right, normalized to non-depleted control) in the ear at week 3 p.i.
1134 in non-depleted (black symbols) or partially depleted (grey symbols) controls versus 100% *Pdpn*-
1135 dependent depleted BM chimeras (blue symbols). **M.** Fraction (left) and MFI (right) of IFNγ^{+} expressing
1136 CD4^{+}CD44^{+} effector T cells from ear tissue (left) in the ear at week 3 p.i. in non-depleted (black
1137 symbols) or partially depleted (grey symbols) controls versus 100% *Pdpn*-dependent depleted BM
1138 chimeras (blue symbols). Each symbol in (L) and (M) represents one individual mouse ear, data
1139 representative of two independent experiments. Horizontal lines denote the median. **, $p<0.01$
1140 according to Mann-Whitney test.
1141
1142 **Figure 4. Fibroblast-produced IL-7 contributes to pathogen persistence and suppression of IFNγ**
1143 **production in effector T cells.**
1144 **A.** Upper panels: H2KB^{+} or PD-L1^{+} fraction and H2KB or PD-L1 MFI of among fibroblasts from mice
1145 reconstituted with *Pdpn-cre* × *Il7r*$^{WT/WT}$ littermate control BM (black symbols) or *Pdpn-cre* × *Il7r*$^{fl/fl}$ BM

1146 (blue symbols). Data normalized to mice reconstituted with littermate control BM. Lower panels:
1147 H2KB$^+$ or PD-L1$^+$ fraction and H2KB or PD-L1 MFI of among fibroblasts from non-depleted control
1148 (black symbols) or *Pdpn*-dependent 100% depleted (blue symbols) ear infections. Each symbol
1149 represents one individual mouse ear. Data normalized to non-depleted control animals. Horizontal lines
1150 denote the mean. ***, p<0.001; **, p<0.01; *, p<0.05 according to unpaired t-test. Data shown
1151 correspond to the experiments shown in fig. 3C-E, , and K, respectively. **B.** Expression of *Il7* within *L.*
1152 *major*-infected (week 3 p.i.) and non-infected ear tissue. Expression as determined by ΔΔCT between
1153 *Il7* and *Hprt* qPCR. CT values are corrected according to the mean difference in RNA extracted (see fig.
1154 S4C). Each symbol represents one individual mouse ear. Horizontal lines denote the mean. *, p<0.05
1155 according to unpaired t-test. **C.** Expression level of *Prrx* among fibroblasts, LEC, BEC and PDPN$^-$CD31$^-$
1156 non-immune cells within *L. major*-infected ear tissue at week 3 p.i.. Expression as determined by ΔΔCT
1157 between *Prrx* and *Hprt* qPCR followed by normalization to PDPN$^-$CD31$^-$ cells. Each symbol represents
1158 one individual mouse ear. Horizontal lines denote the mean. ****, p<0.0001 according to one-way
1159 ANOVA multiple comparison with Dunnett's post-test. Data in (A-C) pooled from two independent
1160 experiments. **D.** Proportion of fibroblasts, LEC, and BEC among CD45$^-$TER119$^-$7AAD$^-$ cells within the
1161 *L. major* infected ear at week 3 p.i.. Each symbol represents one individual mouse ear. Horizontal lines
1162 denote the mean. ****, p<0.0001 according to one-way ANOVA multiple comparison with Dunnett's
1163 post-test. **E.** Experimental setup to test for *Prrx*-expressing fibroblasts as a necessary source of IL-7 to
1164 promote *Lm*^{lo}Mo3 mediated suppression of CD4$^+$ T cell responses in the *L. major* infected ear tissue. **F.**
1165 Expression level of *Il7* among fibroblasts, LEC, and BEC within *L. major*-infected ear tissue from
1166 littermate control (*Prrx-Cre* × *Il7*$^{wt/wt}$) (black symbols) and *Prrx-cre* × *Il7*$^{fl/fl}$ (blue symbols). Expression
1167 as determined by ΔCT between *Il7* and *Hprt* qPCR. **G.** Left: the fraction of *L. major* infected cells
1168 among recruited monocytes in the ear tissue at week 3 p.i., littermate control (*Prrx-Cre* × *Il7*$^{wt/wt}$) (filled
1169 symbols) and *Prrx-cre* × *Il7*$^{fl/fl}$ (open symbols). Differently shaded symbols represent two independent
1170 experiments. Each symbol represents one individual mouse ear. Horizontal lines denote the median.
1171 ***, p<0.001 according to two-way ANOVA comparing genotypes. Right: Limiting dilution assay
1172 (LDA) of *L. major* tissue burden in the ear. Data normalized to littermate control animals. **H.** IFNγ$^+$
1173 fraction and MFI of IFNγ signal among effector CD4$^+$ T cells within *L. major*-infected ear at week 3 p.i.

1174 of either littermate control (black symbols) or *Prrx-cre* × *Il7*$^{fl/fl}$ animals (blue symbols). Data normalized
1175 to littermate control animals. Each symbol in (G-I) represents one individual mouse ear, data are from
1176 two independent experiments. Horizontal lines denote the mean. *, p<0.05 according to unpaired t-test.
1177

1178 **Figure 5. IFNγ activates fibroblasts to produce IL-7 depending of the infection amplitude.**
1179 **A**. Proportion of IFNγ^{+} produced by T, NK, and dendritic cells at week 3 p.i. Each symbol represents
1180 one individual mouse ear. Horizontal lines denote the mean. ****, p<0.0001 according to unpaired t-
1181 test. **B.** Expression of the *Il7* cytokine gene in ex vivo cultivated fibroblasts without (black symbols) and
1182 with (red symbols) addition of IFNγ^{+} for 24h. Horizontal lines denote the median. **, p<0.01 according
1183 to Mann-Whitney test. **C.** Experimental setup to test the impact of anti-IFNγ treatment in fibroblasts
1184 within an ongoing *L. major* infection. **D.** Correlation (r^2, with p value indicated) and linear regression
1185 (red line) between *L. major* infection rate (determined by flow cytometry) and *Il7* expression level
1186 (qPCR) in fibroblasts within the infected ear (week 3 p.i.), in either isotype control (black symbols,
1187 upper graph) or anti-IFNγ treated (orange symbols, lower graph) animals. Each symbol represents one
1188 replicate of flow cytometry analysis from six individual infected ears per condition with qPCR of up to
1189 3 pools of 200 fibroblasts sorted from the same infected ear. The vertical dashed line shows the threshold
1190 defined for analyzing highly infected tissues. **E.** Comparison of *Il7* expression in fibroblasts sorted from
1191 tissues with an infection rate above the threshold (dashed line) shown in (D). **F.** H2KB^{+} or PD-L1^{+}
1192 fraction and H2KB or PD-L1 MFI among fibroblasts isolated from week 3 p.i. infected ears of animals
1193 treated with either isotype control (black symbols) or anti-IFNγ antibody (orange symbols). Each symbol
1194 in (E-G) represents one individual mouse ear, horizontal lines denote the mean. ***, p<0.001; **,
1195 p<0.01; *, p<0.05 according to unpaired t-test. Data were collected in two independent experiments.
1196

1197 **Figure 6. Anti-IL-7/IL-7R treatment results in an enhanced immune response against *L. major*.**
1198 **A.** Hypothesis (box) and experimental setup for testing the effects of anti-IL-7/IL-7R treatment during
1199 *L. major* infection. Treatment was applied twice (day 16, 20, black arrows, data shown in panel B-F) or
1200 once (day 18, grey arrow, data shown in panel C). **B-C.** Limiting dilution assay (LDA) of *L. major* tissue
1201 burden in the ear following anti-IL-7/IL-7R treatment normalized to isotype control treated animals (B)

1202 and *L. major* infected cell fraction among recruited monocytes with two-dosage (left panel) or single-
1203 dosage anti-IL-7/IL-7R treatment (right panel) (C). **D.** IFNγ$^+$ fraction (left) and IFNγ MFI (normalized
1204 to isotype control treatment, right) among effector CD4$^+$ T cells isolated from the ears at week 3 p.i. of
1205 either isotype antibody (black symbols) or anti-IL-7R/IL-7 treated animals (blue symbols). **E.** H2KB$^+$
1206 and PD-L1$^+$ fraction among fibroblasts, and the MFI of H2KB or PD-L1 among fibroblasts (normalized
1207 to isotype control animals), either isotype control (black symbols) or anti-IL-7R/IL-7 treated (blue
1208 symbols). **F.** iNOS$^+$ fraction and iNOS MFI (normalized to isotype control animals) among total
1209 recruited monocyte-derived cells (left panel) and infected monocyte-derived cells (right panel), either
1210 isotype control (black symbols) or anti-IL-7R/IL-7 treated samples (blue symbols). Each symbol in (B-
1211 F) represents one individual mouse ear, data pooled from two independent experiments. Horizontal lines
1212 denote the mean. . **, $p<0.01$; *, $p<0.05$ according to unpaired t-test. **G**. Experimental setup to determine
1213 the long-term effects of anti-IL-7/IL-7R treatment. **H.** Infection-associated immune cell recruitment
1214 determined by ear diameter of isotype control-treated (grey) and anti-IL-7/IL-7R treated (blue) animals.
1215 Data were normalized to the mean of the corresponding values of the same ear measured before the
1216 treatment. Bars denote the mean+SD. Each symbol represents one individual ear repeatedly measured
1217 throughout the infection time course. Data obtained from two independent experiments. ****, $p<0.0001$
1218 *, $p<0.05$ according to 2-way ANOVA (treatment, experiment) with Bonferroni post-test. **I.** Limiting
1219 dilution assay (LDA) of *L. major* tissue burden in the ear at week 7 p.i. of animals previously treated
1220 (week 3 p.i.) with isotype control-treated (black symbols) or anti-IL-7/IL-7R treated (blue symbols). **J.**
1221 IFNγ$^+$ fraction among CD4$^+$ T cells isolated from the draining lymph node at week 7 p.i. of animals
1222 previously treated (week 3 p.i.) with either isotype control (black symbols) or anti-IL-7R/IL-7 antibody
1223 (blue symbols). Each symbol in (I-J) represents one individual ear. Data pooled from two independent
1224 experiments and normalized to control animals of each experiment for limiting dilution. Horizontal lines
1225 denote the median. *, $p<0.05$ according unpaired Mann-Whitney test. Each symbol represents one
1226 individual mouse ear. Horizontal lines denote the mean. ***, $p<0.001$; according to unpaired Mann-
1227 Whitney test.
1228
1229

Figure 1

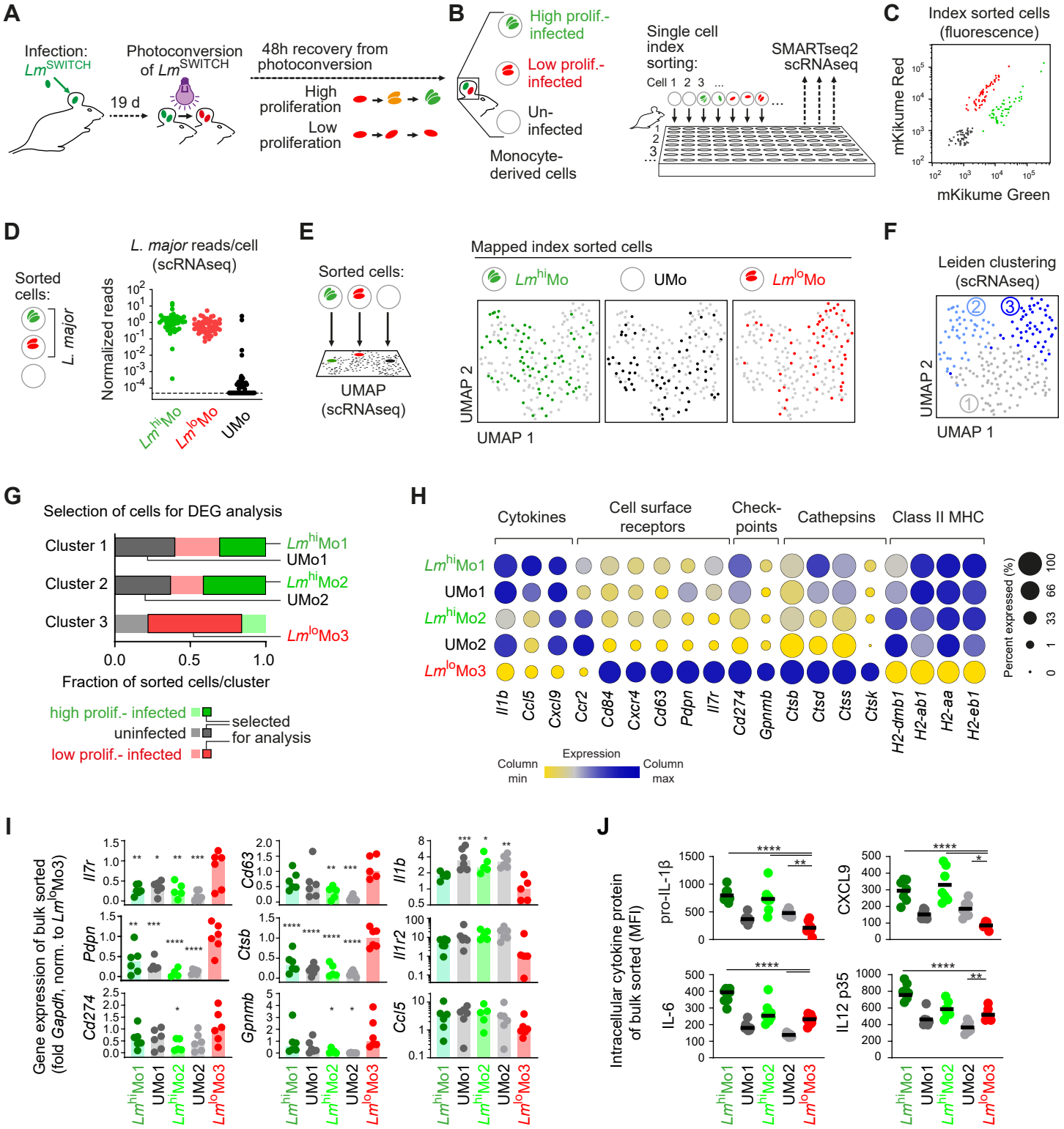
A
Infection:
Lm SWITCH
19 d
Photoconversion of Lm SWITCH
48h recovery from photoconversion
High proliferation
Low proliferation
B
High prolif.- infected
Low prolif.- infected
Un- infected
Monocyte- derived cells
Single cell index sorting:
Cell 1 2 3 ...
SMARTseq2 scRNAseq
C
Index sorted cells (fluorescence)
mKikume Red
mKikume Green
D
Sorted cells:
L. major
L. major reads/cell (scRNAseq)
Normalized reads
Lm hiMo
Lm loMo
UMo
E
Sorted cells:
UMAP (scRNAseq)
Mapped index sorted cells
Lm hiMo
UMo
Lm loMo
UMAP 2
UMAP 1
F
Leiden clustering (scRNAseq)
UMAP 2
UMAP 1
G
Selection of cells for DEG analysis
Cluster 1
Cluster 2
Cluster 3
Lm hiMo1
UMo1
Lm hiMo2
UMo2
Lm loMo3
Fraction of sorted cells/cluster
high prolif.- infected
uninfected
low prolif.- infected
selected for analysis
H
Cytokines
Cell surface receptors
Check- points
Cathepsins
Class II MHC
Lm hiMo1
UMo1
Lm hiMo2
UMo2
Lm loMo3
Il1b
Ccl5
Cxcl9
Ccr2
Cd84
Cxcr4
Cd63
Pdpn
Il7r
Cd274
Gpnmb
Ctsb
Ctsd
Ctss
Ctsk
H2-dmb1
H2-ab1
H2-aa
H2-eb1
Percent expressed (%)
Expression
Column min
Column max
I
Gene expression of bulk sorted (fold Gapdh, norm. to Lm loMo3)
Il7r
Cd63
Il1b
Pdpn
Ctsb
Il1r2
Cd274
Gpnmb
Ccl5
Lm hiMo1
UMo1
Lm hiMo2
UMo2
Lm loMo3
J
Intracellular cytokine protein of bulk sorted (MFI)
pro-IL-1β
CXCL9
IL-6
IL12 p35

Figure 2

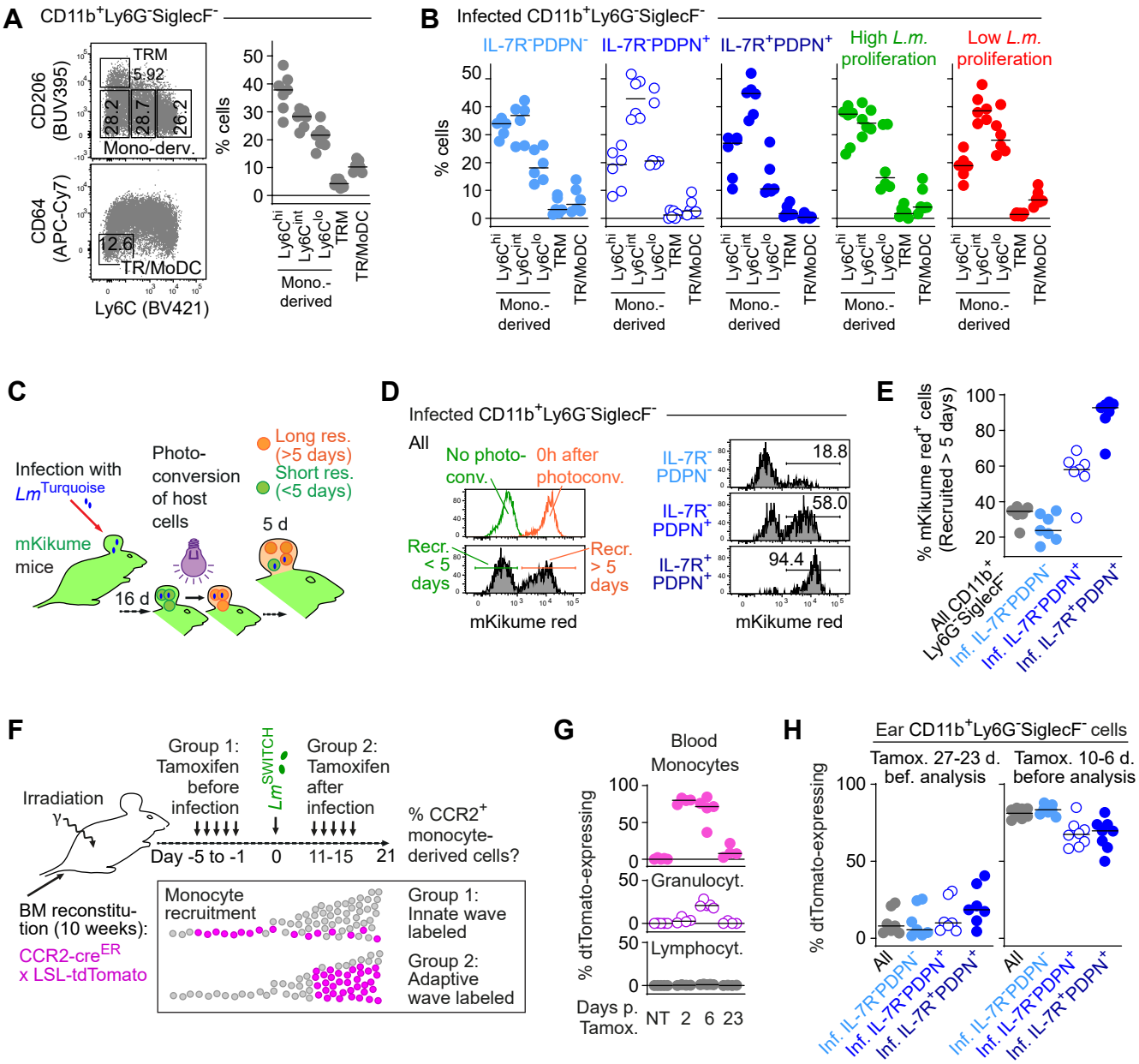
A
CD11b+Ly6G-SiglecF-
CD206 (BUV395)
TRM
5.92
28.2
28.7
26.2
Mono-derv.
CD64 (APC-Cy7)
12.6
TR/MoDC
Ly6C (BV421)
% cells
Ly6Chi
Ly6Cint
Ly6Clo
TRM
TR/MoDC
Mono.-derived
B
Infected CD11b+Ly6G-SiglecF-
IL-7R-PDPN-
IL-7R-PDPN+
IL-7R+PDPN+
High L.m. proliferation
Low L.m. proliferation
C
Infection with
LmTurquoise
mKikume mice
Photo-conversion of host cells
Long res. (>5 days)
Short res. (<5 days)
5 d
16 d
D
Infected CD11b+Ly6G-SiglecF-
All
No photo-conv.
0h after photoconv.
Recr. < 5 days
Recr. > 5 days
IL-7R- PDPN-
IL-7R- PDPN+
IL-7R+ PDPN+
18.8
58.0
94.4
mKikume red
E
% mKikume red+ cells (Recruited > 5 days)
All CD11b+ Ly6G-SiglecF-
Inf. IL-7R-PDPN-
Inf. IL-7R-PDPN+
Inf. IL-7R+PDPN+
F
Irradiation
γ
BM reconstitution (10 weeks):
CCR2-creER x LSL-tdTomato
Group 1: Tamoxifen before infection
LmSWITCH
Group 2: Tamoxifen after infection
Day -5 to -1
0
11-15
21
% CCR2+ monocyte-derived cells?
Monocyte recruitment
Group 1: Innate wave labeled
Group 2: Adaptive wave labeled
G
Blood Monocytes
Granulocyt.
Lymphocyt.
% dtTomato-expressing
Days p. Tamox.
NT
2
6
23
H
Ear CD11b+Ly6G-SiglecF- cells
Tamox. 27-23 d. bef. analysis
Tamox. 10-6 d. before analysis
% dtTomato-expressing
All
Inf. IL-7R-PDPN-
Inf. IL-7R-PDPN+
Inf. IL-7R+PDPN+

Figure 3

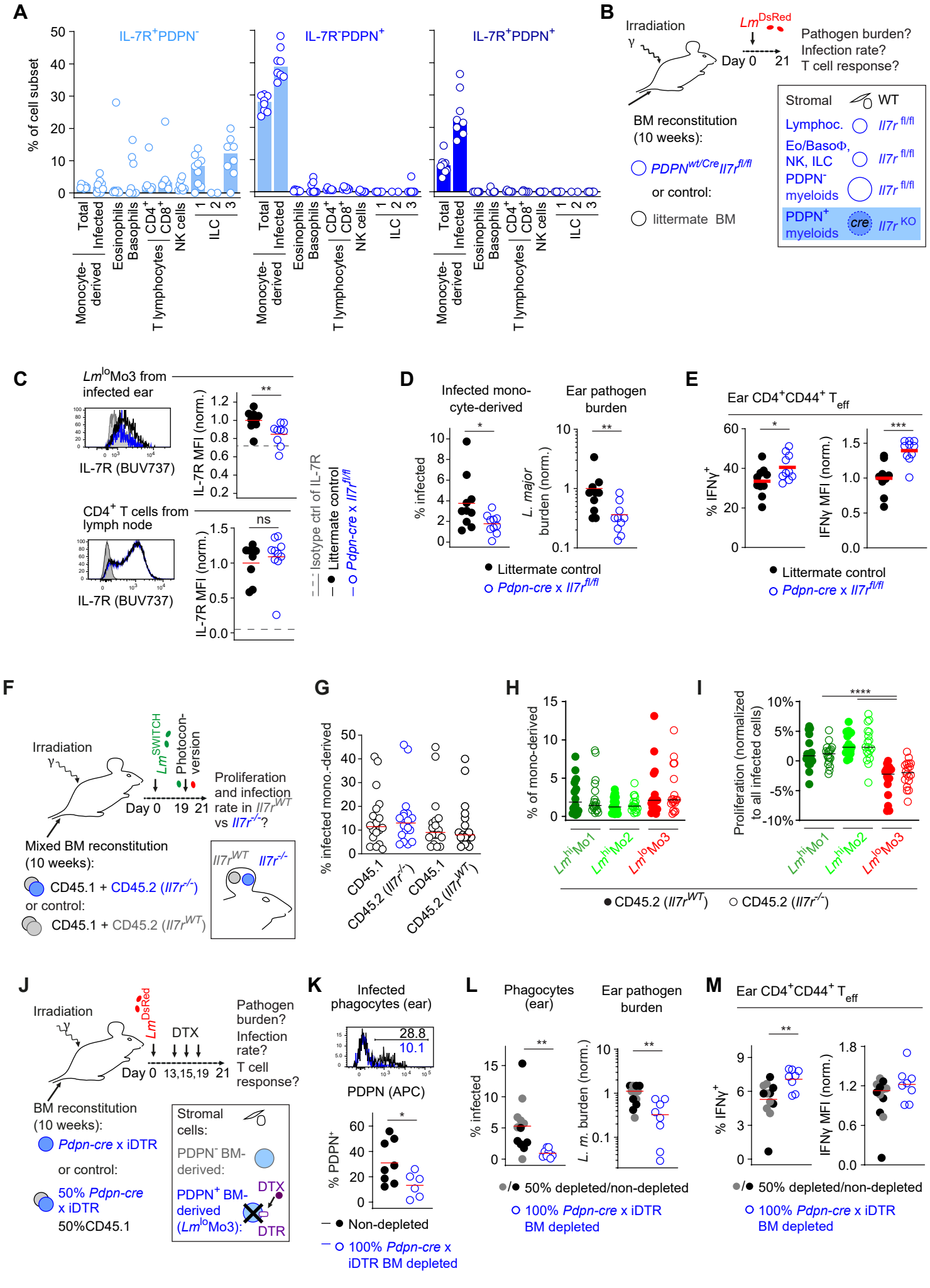
A
IL-7R+PDPN-
IL-7R-PDPN+
IL-7R+PDPN+
% of cell subset
Total
Infected
Monocyte-derived
Eosinophils
Basophils
T lymphocytes
CD4+
CD8+
NK cells
ILC
1
2
3
B
Irradiation
γ
LmDsRed
Day 0
21
Pathogen burden?
Infection rate?
T cell response?
BM reconstitution (10 weeks):
PDPNwt/Cre Il7rfl/fl
or control:
littermate BM
Stromal
WT
Lymphoc.
Il7r fl/fl
Eo/BasoΦ, NK, ILC
PDPN- myeloids
PDPN+ myeloids
cre
Il7r KO
C
LmloMo3 from infected ear
IL-7R (BUV737)
IL-7R MFI (norm.)
**
CD4+ T cells from lymph node
ns
Isotype ctrl of IL-7R
Littermate control
Pdpn-cre x Il7rfl/fl
D
Infected mono-cyte-derived
Ear pathogen burden
% infected
L. major burden (norm.)
*
**
Littermate control
Pdpn-cre x Il7rfl/fl
E
Ear CD4+CD44+ Teff
% IFNγ+
IFNγ MFI (norm.)
*
***
Littermate control
Pdpn-cre x Il7rfl/fl
F
Irradiation
γ
LmSWITCH
Photocon-version
Day 0
19
21
Proliferation and infection rate in Il7rWT vs Il7r-/-?
Mixed BM reconstitution (10 weeks):
CD45.1 + CD45.2 (Il7r-/-)
or control:
CD45.1 + CD45.2 (Il7rWT)
Il7rWT
Il7r-/-
G
% infected mono.-derived
CD45.1
CD45.2 (Il7r-/-)
CD45.1
CD45.2 (Il7rWT)
H
% of mono-derived
LmhiMo1
LmhiMo2
LmloMo3
CD45.2 (Il7rWT)
CD45.2 (Il7r-/-)
I
Proliferation (normalized to all infected cells)
****
LmhiMo1
LmhiMo2
LmloMo3
CD45.2 (Il7rWT)
CD45.2 (Il7r-/-)
J
Irradiation
γ
LmDsRed
DTX
Day 0
13,15,19
21
Pathogen burden?
Infection rate?
T cell response?
BM reconstitution (10 weeks):
Pdpn-cre x iDTR
or control:
50% Pdpn-cre x iDTR
50%CD45.1
Stromal cells:
PDPN- BM-derived:
PDPN+ BM-derived (LmloMo3):
DTX
DTR
K
Infected phagocytes (ear)
28.8
10.1
PDPN (APC)
% PDPN+
*
Non-depleted
100% Pdpn-cre x iDTR BM depleted
L
Phagocytes (ear)
Ear pathogen burden
% infected
L. m. burden (norm.)
**
**
50% depleted/non-depleted
100% Pdpn-cre x iDTR BM depleted
M
Ear CD4+CD44+ Teff
% IFNγ+
IFNγ MFI (norm.)
**
50% depleted/non-depleted
100% Pdpn-cre x iDTR BM depleted

Figure 4

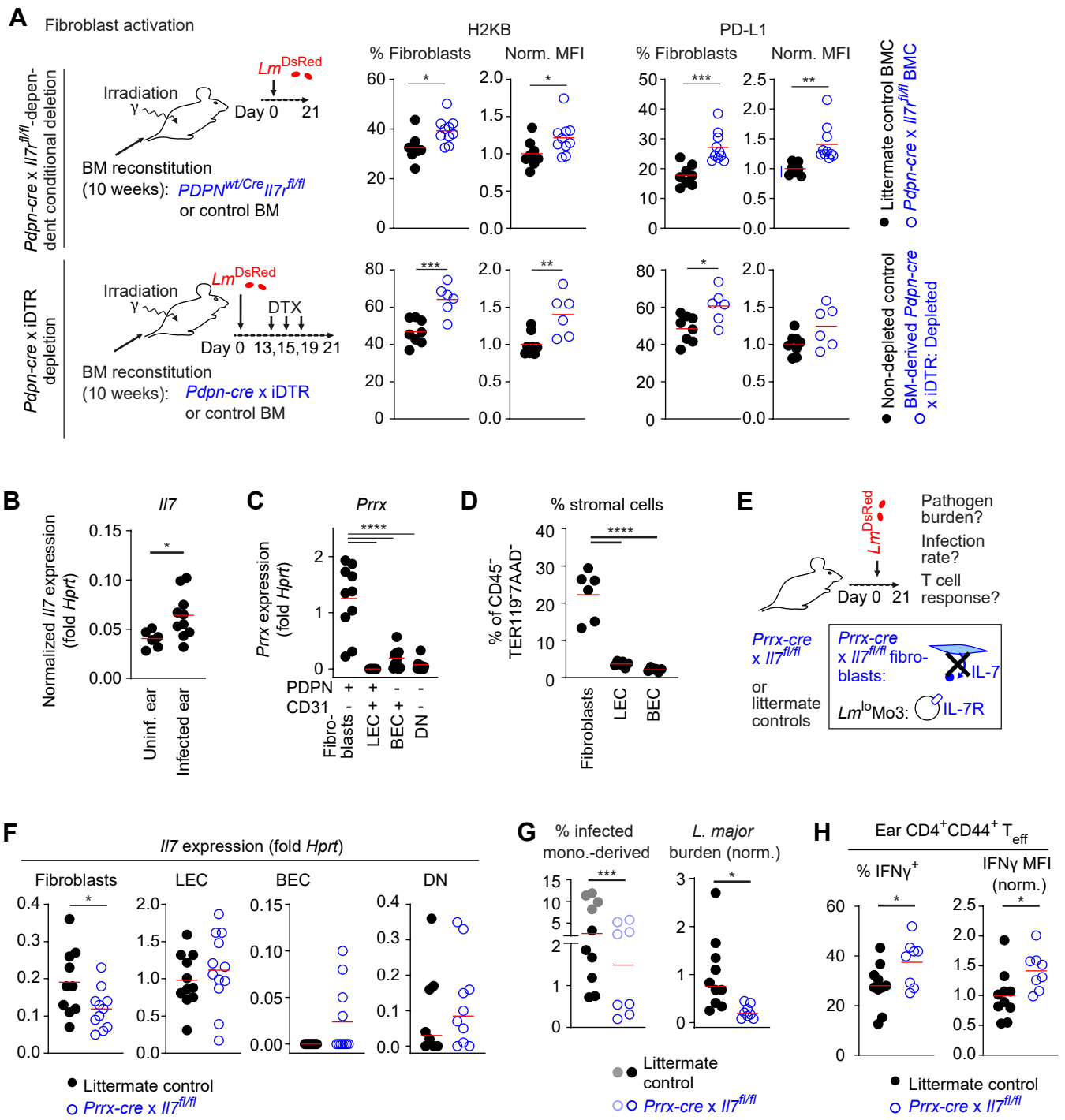
A
Fibroblast activation
H2KB
PD-L1
% Fibroblasts
Norm. MFI
Pdpn-cre x Il7r fl/fl-dependent conditional deletion
Irradiation
γ
Lm DsRed
Day 0
21
BM reconstitution
(10 weeks): PDPN wt/Cre Il7r fl/fl
or control BM
Littermate control BMC
Pdpn-cre x Il7r fl/fl BMC
Pdpn-cre x iDTR depletion
DTX
Day 0 13,15,19 21
Pdpn-cre x iDTR
Non-depleted control
BM-derived Pdpn-cre x iDTR: Depleted
B
Il7
Normalized Il7 expression (fold Hprt)
Uninf. ear
Infected ear
C
Prrx
Prrx expression (fold Hprt)
PDPN
CD31
Fibro-blasts
LEC
BEC
DN
D
% stromal cells
% of CD45- TER119-7AAD-
Fibroblasts
LEC
BEC
E
Pathogen burden?
Infection rate?
T cell response?
Prrx-cre x Il7 fl/fl
or littermate controls
Prrx-cre x Il7 fl/fl fibro-blasts:
IL-7
Lm loMo3:
IL-7R
F
Il7 expression (fold Hprt)
Fibroblasts
LEC
BEC
DN
Littermate control
Prrx-cre x Il7 fl/fl
G
% infected mono.-derived
L. major burden (norm.)
Littermate control
Prrx-cre x Il7 fl/fl
H
Ear CD4+CD44+ Teff
% IFNγ+
IFNγ MFI (norm.)
Littermate control
Prrx-cre x Il7 fl/fl

Figure 5

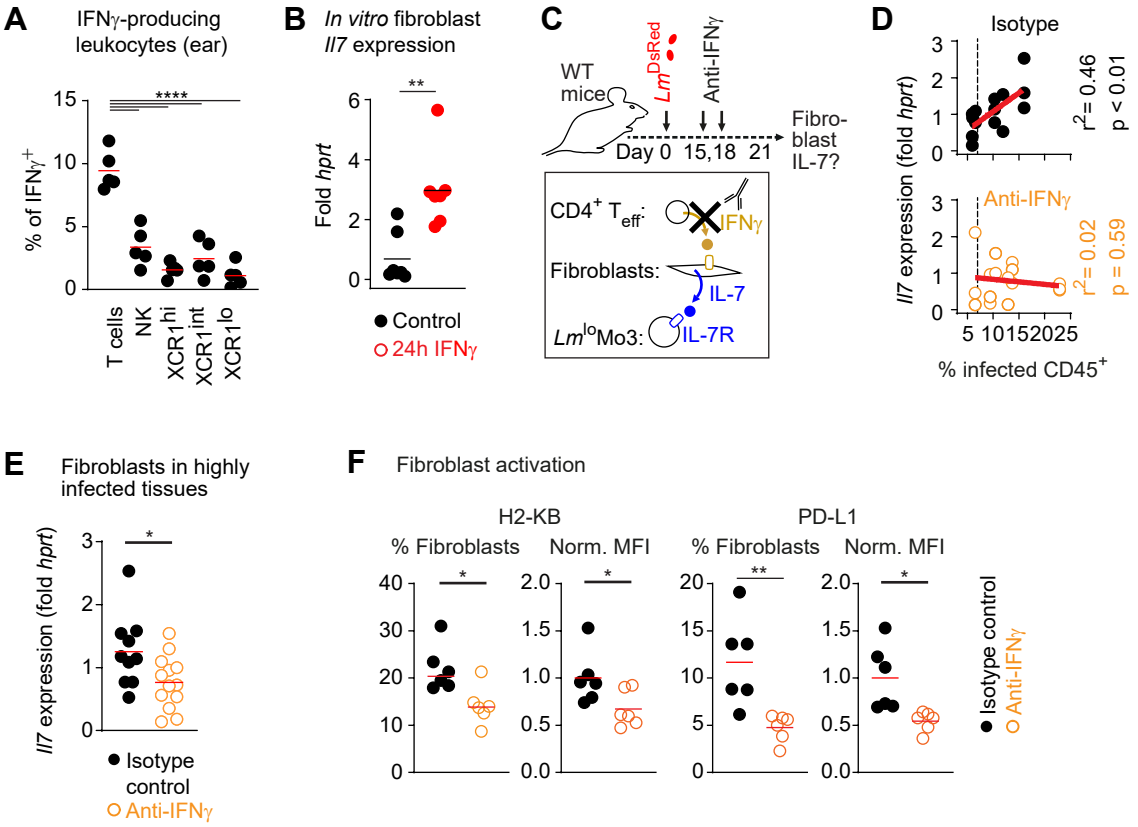
A
IFNγ-producing leukocytes (ear)
% of IFNγ+
****
T cells
NK
XCR1hi
XCR1int
XCR1lo
B
In vitro fibroblast Il7 expression
Fold hprt
**
Control
24h IFNγ
C
WT mice
LmDsRed
Anti-IFNγ
Day 0 15,18 21
Fibro-blast IL-7?
CD4+ Teff:
IFNγ
Fibroblasts:
IL-7
LmloMo3:
IL-7R
D
Isotype
Anti-IFNγ
Il7 expression (fold hprt)
r2= 0.46
p < 0.01
r2= 0.02
p = 0.59
% infected CD45+
E
Fibroblasts in highly infected tissues
Il7 expression (fold hprt)
*
Isotype control
Anti-IFNγ
F
Fibroblast activation
H2-KB
PD-L1
% Fibroblasts
Norm. MFI
Isotype control
Anti-IFNγ

Figure 6

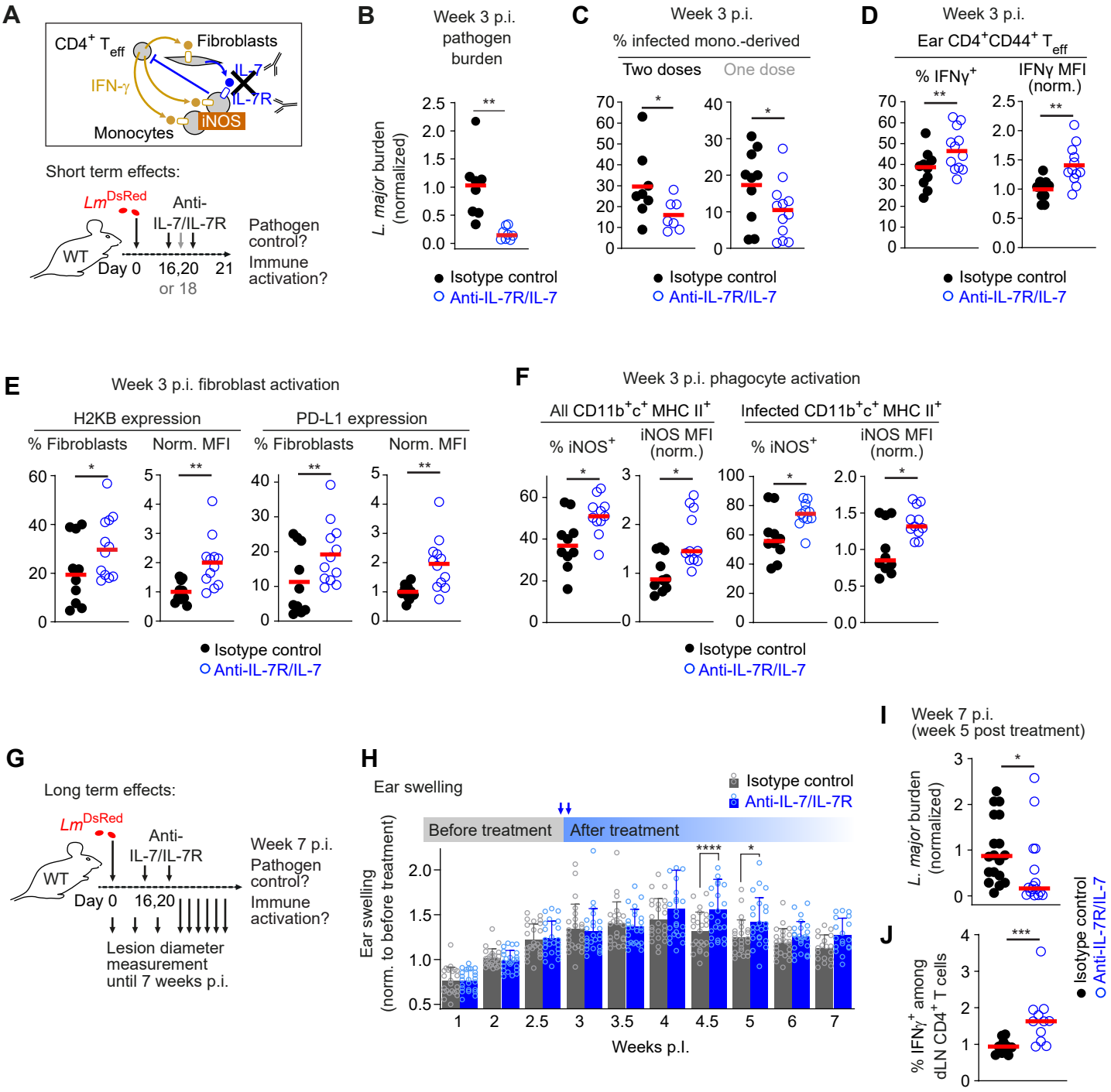
A
CD4+ Teff
Fibroblasts
IL-7
IFN-γ
IL-7R
iNOS
Monocytes
Short term effects:
LmDsRed
Anti-
IL-7/IL-7R
WT
Day 0
16,20
or 18
21
Pathogen control?
Immune activation?
B
Week 3 p.i.
pathogen burden
L. major burden (normalized)
Isotype control
Anti-IL-7R/IL-7
C
Week 3 p.i.
% infected mono.-derived
Two doses
One dose
Isotype control
Anti-IL-7R/IL-7
D
Week 3 p.i.
Ear CD4+CD44+ Teff
% IFNγ+
IFNγ MFI (norm.)
Isotype control
Anti-IL-7R/IL-7
E
Week 3 p.i. fibroblast activation
H2KB expression
PD-L1 expression
% Fibroblasts
Norm. MFI
% Fibroblasts
Norm. MFI
Isotype control
Anti-IL-7R/IL-7
F
Week 3 p.i. phagocyte activation
All CD11b+c+ MHC II+
Infected CD11b+c+ MHC II+
% iNOS+
iNOS MFI (norm.)
% iNOS+
iNOS MFI (norm.)
Isotype control
Anti-IL-7R/IL-7
G
Long term effects:
LmDsRed
Anti-
IL-7/IL-7R
WT
Day 0
16,20
Week 7 p.i.
Pathogen control?
Immune activation?
Lesion diameter measurement until 7 weeks p.i.
H
Ear swelling
Isotype control
Anti-IL-7/IL-7R
Before treatment
After treatment
Ear swelling (norm. to before treatment)
Weeks p.i.
I
Week 7 p.i.
(week 5 post treatment)
L. major burden (normalized)
J
% IFNγ+ among dLN CD4+ T cells
Isotype control
Anti-IL-7R/IL-7